Geoscience Frontiers 17 (2026) 102207

Contents lists available at ScienceDirect

Geoscience Frontiers

journal homepage: www.elsevier.com/locate/gsf

Research Paper

The Messinian halite facies: Insights into halite crystallisation and depositional environments using geochemical, petrographic and fluid inclusion studies

Mara Cipriani [a,*], Alessandra Costanzo [b], Martin Feely [b], Adriano Guido [a], Massimo D'Antonio [c], Giovanni Vespasiano [a], Sandro Donato [d,e,f], Giuseppe Cianflone [a], Giuseppe Maruca [a], Carmine Apollaro [a], Francesca Alessandro [g], Francesco Perri [a], Rocco Dominici [a]

[a] Department of Biology, Ecology and Earth Science, University of Calabria, Arcavacata di Rende 87036 Rende, Italy
[b] Earth and Ocean Sciences, School of Natural Sciences, University of Galway H91 TK33 Galway, Ireland
[c] Department of Earth, Environmental and Resources Sciences, University of Naples Federico II, 80126 Napoli, Italy
[d] Department of Mathematics and Computer Science, University of Calabria, Arcavacata di Rende, 87036, Italy
[e] Department of Physics and STAR-Lab, University of Calabria, Arcavacata di Rende, 87036, Italy
[f] INFN, Division of Frascati, Frascati, RM 00044, Italy
[g] National Research Council of Italy, Institute on Membrane Technology, CNR-ITM, Arcavacata di Rende, 87036, Italy

ARTICLE INFO

Article history:
Received 12 May 2025
Revised 10 October 2025
Accepted 31 October 2025
Available online 4 November 2025

Keywords:
Messinian Salinity Crisis
Salt deposits
Facies analysis
Evaporite formation
Organic matter

ABSTRACT

The Crotone Basin (Calabria, Southern Italy) is a representative area in the Italian peninsula where Messinian halite deposits preserve three distinct crystal facies: (i) *banded* composed of cumulate halite and mud-rich interlayers, (ii) *white* consisting of bottom-growth crystals with chevron fabrics, and (iii) *transparent* made up of massive, optically pure crystals. The transparent facies appears to be undocumented in other Mediterranean Messinian basins, offering new perspective on halite crystallisation under variable environmental conditions. Microscopic observations (optical and scanning electron microscopy), supported by high-resolution 3D imaging through synchrotron-based X-ray microtomography, revealed a lack of pervasive recrystallisation in all facies, enabling the non-destructive visualisation of internal fabrics and inclusions. These methods provided critical insights into halite growth dynamics and the environmental conditions prevailing during deposition.

Microthermometric data indicated that all halite crystals precipitated from a NaCl-$MgCl_2$-H_2O salt-water system under extreme evaporative conditions, with fluid salinity exceeding 340 ‰ – 360 ‰ and a distinct brine temperature for each facies (~35 °C in the banded, ~45 °C in the white, and ~ 20 °C in the transparent). Strontium isotope ratios ($^{87}Sr/^{86}Sr$) placed halite formation within the TG14-TG12 interval (ca. 5.61 – 5.55 Ma), with progressively increasing values from banded to transparent facies, suggesting enhanced continental input and brine dilution in the later stages of deposition.

Organic matter was detected both in primary fluid inclusions and within the halite lattice, particularly in the white and transparent facies. Raman spectroscopy and UV-epifluorescence revealed amorphous organic compounds, including carotenoids and aliphatic functional groups such as methyl and methylene, which are commonly associated with microbial activity. These findings suggested that organic-rich brines may have played an active role in crystal nucleation and growth dynamics. The chemical immaturity and heterogeneous distribution of organic compounds imply a combination of autochthonous microbial input and episodic allochthonous influx, pointing to complex organic-mineral interactions during halite formation.

The coexistence of three petrographically distinct halite facies within a confined area, each linked to specific environmental and geochemical conditions, supports the view that halite precipitation was modulated by fluctuations in hydrological balance, brine composition, and organic matter availability. These data contribute to a better understanding of the environmental and geochemical processes that controlled evaporite deposition during the Messinian Salinity Crisis.

* Corresponding author.
E-mail addresses: mara.cipriani@unical.it (M. Cipriani), alessandra.costanzo@universityofgalway.ie (A. Costanzo), martin.feely@universityofgalway.ie (M. Feely), adriano.guido@unical.it (A. Guido), massimo.dantonio@unina.it (M. D'Antonio), giovanni.vespasiano@unical.it (G. Vespasiano), sandro.donato@unical.it (S. Donato), giuseppe.cianflone@unical.it (G. Cianflone), giuseppe.maruca@unical.it (G. Maruca), carmine.apollaro@unical.it (C. Apollaro), francesca.alessandro@unical.it (F. Alessandro), francesco.perri@unical.it (F. Perri), rocco.dominici@unical.it (R. Dominici).

https://doi.org/10.1016/j.gsf.2025.102207

1. Introduction

During the Messinian age (5.97 – 5.33 Ma), the Mediterranean area was characterised by a catastrophic event (Hsü et al., 1977; Krijgsman et al., 1999; Fauquette et al., 2006; Lugli et al., 2015), known as the Messinian Salinity Crisis (MSC). This resulted from two simultaneous factors: (i) a slow paleogeographic evolution driven by plate tectonics, which progressively led to the restriction of marine gateways and to the temporary decrease reduction of connections between the Mediterranean Sea and the Atlantic Ocean, and (ii) an eustatic fall in the sea level linked with global cooling (Garcia-Castellanos and Villasenõr, 2011; Flecker et al., 2015; Ohneiser et al., 2015). This relatively recent (6 Ma) and very rapid event (short time window of ca. 600.000 years) changed the chemistry of the Mediterranean Sea and produced a permanent impact on both terrestrial and marine ecosystems of the entire area (CIESM, 2008; Agiadi et al., 2024).

The MSC led to the deposition of kilometres-thick evaporite units, including carbonates, gypsum and halite, across several Mediterranean basins. Numerous studies have investigated various aspects of these deposits, with particular attention to depositional environments influenced by regional tectonics and climate, as well as changes in the hydrological balance, often assessed through $^{87}Sr/^{86}Sr$ isotopic analyses (Müller and Mueller, 1991; Flecker et al., 2002; Flecker and Ellam, 2006; Gladstone et al., 2007; Guido et al., 2007; Manzi et al., 2009, 2011; Lugli et al., 2010; Topper et al., 2011; García-Veigas et al., 2013; Topper and Meijer, 2013; Birgel et al., 2014; Roveri et al., 2014; Warren, 2006; Costanzo et al., 2019; Cipriani et al., 2021, 2023a, 2024a; Natalicchio et al., 2014, 2021; Perri et al., 2023, 2024; Aloisi et al., 2024; Krijgsman et al., 2024; Dominici et al., 2025). Halite deposits are one of the most important evaporite rocks from both scientific and economic perspectives (Warren, 2006; Urai and Spiers, 2007; Adamuszek et al., 2021) due to their: (i) abundance, with deposits reaching kilometric thickness, (ii) wide applications in urban and industrial sectors (*e.g.*, mining, construction, civil engineering), and (iii) role in paleoenvironmental reconstruction. The considerable diversity in the conditions of ancient salt accumulation, which often significantly differ from those in modern times, makes the paleogeography of ancient evaporite basins frequently a topic of intense debate. An important contribution is provided by primary fluid inclusions trapped within evaporite crystals representing microreservoirs of water from ancient basins. Their physicochemical features can provide valuable information for reconstructing the paleoenvironmental conditions and mechanisms of halite crystallisation (Davis et al., 1990; Bein et al., 1991; Lowenstein et al., 1998, 2001; Horita et al., 2002; Brennan et al., 2004; García-Veigas et al., 2013; Lugli et al., 2015; Galamay et al., 2023), whereas, secondary fluid inclusions offer insights into post-depositional processes, such as recrystallisation, fluid migration, and later diagenetic events (Schléder and Urai, 2005; Urai and Spiers, 2007; Debois et al., 2012). Messinian evaporites can also preserve organic matter and potential microbial remnants within fluid inclusions, offering additional data to past ecological and environmental conditions (CIESM, 2008). However, studies specifically addressing these aspects in halite are still relatively rare, making them a valuable but currently limited source of paleoenvironmental information (Wierzchos et al., 2006; Hoffmann et al., 2021; Vreeland et al., 2024).

To better constrain the crystallisation and depositional conditions of the halite facies, the present work focuses on two main objectives:

(1) to discriminate the origin (primary or secondary) of the different textures, types and sizes of the halite crystals belonging to the banded, white and transparent facies, based on detailed petrographic analyses (optical microscopy, scanning electron microscopy and synchrotron radiation X-ray computed microtomography);
(2) to clarify the precipitation conditions and determine the origin of the different halite facies in relation to environmental parameters (*e.g.*, brine chemistry, depositional depth, and mineralization processes), chemical analyses were performed on halite crystals and their fluid inclusions. These analyses included Raman spectroscopy, scanning electron microscopy coupled with energy-dispersive X-ray spectrometry, and thermal ionization mass spectrometry for Sr-isotopic ratio determination.

Altogether, the multidisciplinary dataset provides a solid framework for interpreting the environmental conditions that governed halite deposition in the Crotone Basin during the Messinian Salinity Crisis.

1.1. Halite deposits of the Crotone Basin

The halite deposits of the Crotone Basin (Calabria, southern Italy), although already known in 60 s (see Roda, 1964), were only investigated for mineral exploitation. Forty years later, petrographic studies on these crystals were conducted by Lugli et al. (2007) and Speranza et al. (2013, 2016). Lugli et al. (2007) recognised two primary halite facies in the Zinga area and one in the salt mining areas of Belvedere di Spinello, located in the north-east and south-east sectors, respectively. These facies, made of micro- and macro-crystalline halite, were called banded, white and clear. Banded and white facies were sampled from exposed outcrops, whereas the clear facies were documented from drill cores. Although halite facies were strongly modified by folding and recrystallisation, owing to burial and subsequent uplift Lugli et al. (2007) suggested that: (a) the banded facies, made of cumulate crystals, were deposited in a salt pan and a saline mudflat; (b) the white facies, called bottom-growth crystals, were probably deposited in a saline lake which underwent phases of desiccation; and (c) the clear facies were a product of displacive halite overgrowth in a saline mudflat after initial subaqueous nucleation. Speranza et al. (2013, 2016) investigated halite deposits from the Zinga and Verzino areas to elucidate the mechanical and rheological properties of the rock salt. The authors conducted the first microthermometric study on fluid inclusions from the white facies in the Zinga area, estimating a trapping temperature of ~ 18 °C. These studies led to the first elaboration of environmental formations.

These deposits represent an important key for the reconstruction of the stratigraphic architecture, as well as the paleomorphological and paleo-environmental conditions of the Crotone Basin during the Messinian age. Moreover, studying these deposits provides insight into possible future implications since their presence could favour both rapid ground deformation (subsidence) due to their variability in petrographic features (*e.g.*, Cipriani et al.,

2024a) and affect the quality of the local water resource. As reported by Vespasiano et al. (2021, 2023), the widespread presence of such units can promote the development of extremely saline waters affecting the overall quality of aquifers.

2. Geological setting

The Crotone Basin (CB – Fig. 1) is a Neogene wedge-top basin of the southern Italy foreland basin system located along the Ionian side of the Calabria Arc (Roda, 1964; Van Dijk et al., 2000; Barone et al., 2008; Borrelli et al., 2022). In this basin, Zecchin et al. (2020) recognised three first-order sequences named CB_1 (Serravallian-Messinian), CB_2 (uppermost Messinian-Zanclean), and CB_3 (Piacenzian-upper Pleistocene).

The sequence CB_1, covering the Sila Unit (crystalline basement) through a basal unconformity in the western margin of the Crotone Basin, is composed of: (a) the San Nicola Formation (continental deposits), (b) the Ponda Group including the Ponda Clay Formation (shelf to slope marine deposits, mainly clay with sandy and gravelly turbidites), (c) the Hera Lacinia Formation (deep-marine turbiditic deposits), (d) the Monte Anastasia Sandstone (sandstone deposits), (e) the Tripoli Formation (diatomite-rich pelagic deposits), (f) the Evaporite Formation (resedimented gypsum, microbial limestones, and basin-centred halite deposits) and (g) the Petilia Policastro Formation (brackish deposits with siliciclastic and clastic gypsum).

The sequence CB_2, which extends from the uppermost Messinian to Zanclean, records the transition from restricted to fully marine conditions after the Messinian Salinity Crisis. It is composed of: (a) the Carvane Group (continental to lagoonal deposits), (b) the Cavalieri Marl (claystones and siltstones) and (c) the Zinga Group (shallow-marine to fluvio-deltaic deposits).

The sequence CB_3, from the Piacenzian to the upper Pleistocene, reflects coastal progradation, glacio-eustatic fluctuations, and regional uplift. It includes: (a) the Spartizzo Clay (lagoonal deposits), (b) the Scandale Sandstone (sandstones and conglomerates); (c) the Cutro Clay (claystones and siltstones), (d) the San Mauro Sandstone (shallow-marine to fluvial deposits), (e) the Serra Mulara Formation (submarine canyon fill with fining-upward sequences) and (f) terrace deposits (mixed marine to continental sediments).

These three sedimentary sequences reflect the complex interplay between tectonics, sea-level changes, and evaporitic conditions that shaped the Neogene-Quaternary evolution of the Crotone Basin. Among them, the CB_1 sequence preserves extensive evidence of Messinian evaporite deposition, including a thick (up to 300 m) halite-bearing interval (Lugli et al., 2007). In details, Messinian halite deposits outcrops in three distinct areas: Coste del Sale, Zinga, and Verzino (Fig. 1). The Coste del Sale hosts a single, well-preserved halite body and represents the only area in Calabria where the original stratigraphic position of the halite, above the Tripoli Formation, can be directly observed. This study presents

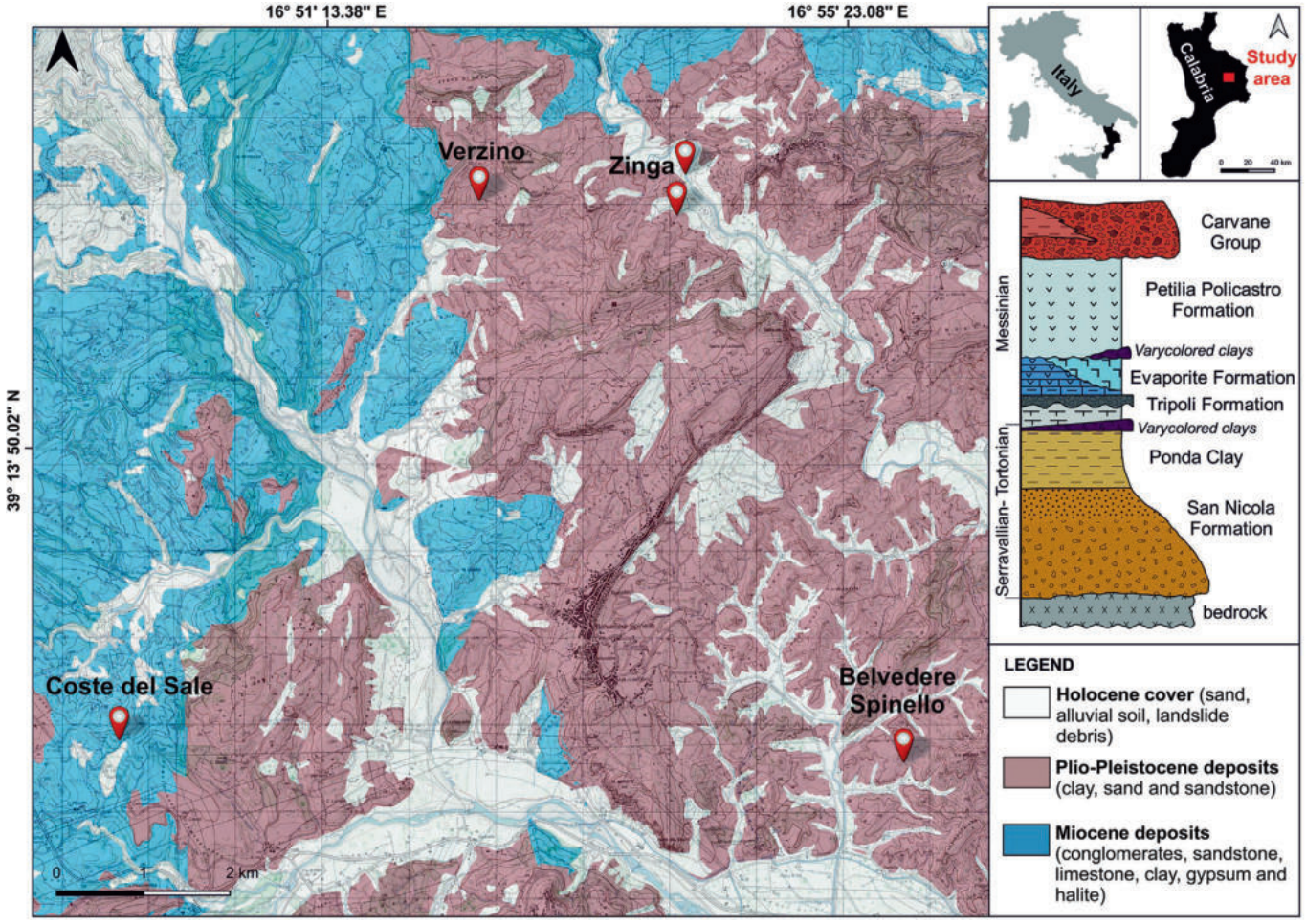

Fig. 1. Geological map and general stratigraphic column of the Crotone Basin (eastern Calabria). In the map the halite deposits outcropping in the Coste del Sale, Zinga and Verzino areas and the salt mine located in the Belvedere Spinello are reported (modified after Barone et al., 2008). In the Zinga e Verzino areas the Miocene evaporitic deposit are covered by Plio-Pleistocene normal marine deposits.

the first documentation and analysis of this deposit, which offers an opportunity to observe undisturbed *in situ* evaporite stratigraphy. In contrast, the halite outcrops at Zinga and Verzino correspond to salt domes that have intruded into overlying late Messinian and Pliocene sediments. Previously described by Lugli et al. (2007), they preserve clear evidence of diapiric activity.

3. Materials and analytical methods

The sampling was preceded by a macroscopic observation of the halite deposits exposed in three distinct areas of the Crotone Basin: Coste del Sale (CS), Zinga (Zi), and Verzino (Ve). All three sites preserve halite belonging to the banded facies, characterised by microcrystalline halite. In addition, the Zinga area also shows deposits of macrocrystalline halite belonging to white facies and transparent facies.

Sixteen samples were selected from the banded facies collected across all three study areas: CS-01 to CS-04, Zi-01 to Zi-06, and Ve-01 to Ve-06 (Table 1), while eight samples, made of macrocrystalline crystals and belonging to the white and transparent facies (Zi-07 to Zi-09; Zi-10 to Zi-14; Table 1), were collected from the Zinga area.

Halite samples were sent to the ALS Petrophysics Laboratory (Normandy) to obtain fluid inclusion wafers (~150 μm in thickness), suitable for petrographic and microthermometric analyses aimed at characterising the composition and entrapment conditions of primary fluid inclusions.

3.1. Optical microscopy

Petrographic and fluid inclusions studies were carried out in the Geofluids Research Laboratory at the University of Galway (Ireland) and the Department of Biology, Ecology and Earth Science of the University of Calabria (Italy). Petrographic investigation was carried out using transmitted light microscopy on a Nikon Eclipse E200 polarizing microscope, at various magnifications (4 ×, 10×, 40×, 60×). UV-epifluorescence were used to discriminate the presence and distribution of organic compounds in the crystal's lattice, between halite crystals and fluid inclusions, through incident light emitted by a Hg high-pressure vapor bulb, attached to a Zeiss Axioplan II Imaging optical microscope, with high-performance wide bandpass filters, used as a parameter of fluorescence intensity (band-pass filter 436/10 nm/long-pass filter 470 nm, no. 488006, for the green light; and band-pass filter 450 490 nm/long-pass filter 515 nm, no. 488009, for the yellow light) (Guido et al., 2012, 2019a,b; Cipriani et al., 2023b, 2024b). This technique was used also to detect hydrocarbon-bearing fluid inclusions.

3.2. Electron microscopy

Morphological observations and semi-quantitative analyses using Scanning Electron Microscopy coupled with Energy Dispersive Spectroscopy (SEM-EDS) were conducted on selected halite crystals from all three facies. The investigations focused on (i) pure halite crystals, (ii) halite crystals displaying trails of fluid inclusions, (iii) amorphous organic material predominantly recognised in microcrystalline halite, and (iv) solid phases trapped within Type 3 fluid inclusions. These analyses aimed to characterise both crystal textures and the associated mineral and organic components across the different facies.

The SEM apparatus utilized was an Ultra High-Resolution SEM (UHR-SEM) – ZEISS CrossBeam 350 under the following condition: resolution 123 eV, high voltage 10 keV, probe current 100 pA and working distance 11 mm. The analysed samples were polished with 0.25 μm diamond-impregnated surfaces and carbon-coated (about 250 Å). Mineralogical and chemical compositions were determined under the following settings: voltage 15 keV, probe current 60 μm, working distance 12 mm, take-off angle 40°, and live time 30 s. The standardless quantitative analysis was checked on the SPI no. 02757-AB serial 4AK standard and was collected through the AMETEK APEX software suite V2.

3.3. Raman spectroscopy

All Raman spectra were recorded at room temperature using a NRS-5500 spectrometer (JascoCorp., Tokyo, Japan) with a 532-nm laser wavelength, 100 × objective and a power of 0.3 mW to avoid damage of the samples. Data acquisition and spectra treatment were carried out with the commercially available program LabSpecv7.02 (HORIBA Jobin Yvon GmbH). Raman analysis was performed on the crystal lattices of massive halite crystals (white and transparent facies), both inside and away from the FI trails, as well as on 35 primary FI types 1 (monophase liquid rich) and 3 (multiphase assemblages), to investigate the brine composition and the mineralogy of the solids trapped within the inclusions.

3.4. Microthermometry

Microthermometric analyses were conducted on twenty-four double-side polished wafers prepared from both microcrystalline and macrocrystalline halite samples. The measurements were performed using a Linkam THMSG 600 heating and cooling stage mounted on an Olympus BX51 transmitted light microscope (with a range of objective lenses including a 100 × lens). The speed of heating was from 1 to 5 °C/min, reduced to as slow as 0.1 °C/min when bubbles were close to homogenization, and a cooling rate of 0.5 to 3 °C/min. Only one stress cycle, ranging from –80 °C

Table 1
Summary list on the main information based on field observations, on halite sampled crystals and on previous works (n.d. = no data).

Sampling area	Halite facies	Crystals	Samples name	Previous researches
Coste del Sale	Banded	Microcrystalline	CS-01, CS-02, CS-03, CS-04	n.d.
Zinga	Banded	Microcrystalline	Zi-01, Zi-02, Zi-03, Zi-04, Zi-05, Zi-06	n.d.
	White	Macrocrystalline (Bottom-growth)	Zi-07, Zi-08, Zi-09	Speranza et al. (2013)
	Transparent	Macrocrystalline (Massive)	Zi-10, Zi-11, Zi-12, Zi-13, Zi-14	n.d.
Verzino	Banded	Microcrystalline	Ve-01, Ve-02, Ve-03, Ve-04, Ve-05, Ve-06	Lugli et al. (2007)

to +50 °C, was conducted because multiple cycles showed an error of approximately ±3 °C for each repetition in the temperature of homogenization (T_H – temperature of the original brine). The temperature of first melting (T_{FM}), according to Shepherd et al. (1985), was recorded to obtain the salt system in which halite crystals formed with an error of ±1 °C. Although newer methods have recently emerged (Guillerm et al., 2020), this study employed the method proposed by Speranza et al. (2013), which has proven particularly useful for analysing a similar deposit, allowing for a direct comparison of the data. The results provided the temperatures at which phase changes take place (*e.g.*, solid melting to liquid or liquid becoming vapour) during cooling-heating cycles. These temperatures are indicative of the fluid composition trapped in the individual inclusion (Shepherd et al., 1985).

Microthermometric analyses were performed exclusively on Type 1 and Type 2 primary fluid inclusions, which consist of monophase liquid rich and two-phase liquid + vapour respectively, as they are considered the most reliable for reconstructing trapping conditions. In contrast, Type 3 inclusions, characterised by multiphase assemblages (liquid ± vapor ± solid ± organic matter), were excluded from the analysis. Although some authors have performed microthermometry on multiphase inclusions when the identity of the solid phases was well constrained (Roedder, 1984; Sterner et al., 1988; Davis et al., 1990; Goldstein, 2001), the presence of accidental solids or daughter minerals can complicate interpretation. In particular, Multiphase inclusions containing organic matter are generally not recommended for microthermometric studies, and the reliability of such measurements remains a matter of debate.

3.5. Synchrotron radiation X-ray computed microtomography (SR X-ray μCT)

3D petrophysical acquisitions on two crystals belonging to the white (Zi-08) and transparent facies (Zi-14) were conducted at the SYRMEP beamline (Dullin et al., 2021) at the Elettra Synchrotron facility in Trieste (Italy). Utilizing the free-space propagation-based phase-contrast imaging modality (PBI) (Brombal et al., 2018), these acquisitions harnessed a polychromatic spectrum spanning [8.5 40] keV, generated by one of the bending magnets of the storage ring. This spectrum underwent filtration to eliminate low-energy components, achieved through 1.5 mm of Silicon and 1 mm of Aluminium, resulting in a beam mean energy of about 24 keV. The imaging setup featured a Hamamatsu sCMOS detector paired with a GGG: Eu scintillator screen, with a thickness of 17 μm, alongside a high numerical optic aperture allowing adjustment of the pixel size within the range of 0.9 to 6.5 μm. For the acquisitions detailed in this paper, a pixel size of 2.5 μm was employed. To capitalize on the phase-contrast effect, the propagation distance between sample and detector was set to 10 cm (Donato et al., 2022). Specimens underwent imaging with 1800 projections captured over 180 degrees, each with an exposure time of 2 s per projection. Due to sample lengths exceeding the field of view (with the beam height, at full width at half maximum, measuring 4.25 mm), scans were obtained at overlapping positions along the specimen axis to ensure comprehensive morphology reconstruction.

Image reconstruction utilized the SYRMEP Tomo Project (STP) software suite (Brun et al., 2015), employing the Filtered Back-Projections (FBP) algorithm (Kak et al., 2002) and removal of ring artifacts (Rivers, 1998). To enhance segmentation reliability and maximize morphological analysis in phase-contrast SR-μCT, we applied a single-distance phase-retrieval algorithm based on the transport of intensity equation (Paganin et al., 2002) to acquired sample projection images before reconstruction. With a parameter value of 150 for $\delta/\beta = \gamma$, manually optimized to preserve microstructural features, being δ and β, respectively, the real and imaginary part of the complex refractive index.

Image segmentation employed Avizo® 9.3 commercial software on both specimens, with merged stacks of reconstructed images from various vertical acquisitions for comprehensive analysis. Volumes of interest, sized at 3.3 mm × 4.0 mm × 17.2 mm and 4.0 m m × 7.8 mm × 8.2 mm, were extracted from the core of the specimen volume, representing respectively the white and transparent specimens. These were segmented using an automatic thresholding algorithm (Otsu, 1979) in a two-step process. The first aim is to distinguish between the solid and porous phases (voids and FI), and the second to further differentiate between voids and FIs.

3.6. Isotopic analyses

Strontium isotopic analysis was carried out on five representative samples at the Department of Earth, Environment and Resources Sciences of the University of Naples Federico II. Samples treatment for Sr separation has been carried out in an ISO 6 class clean room; $^{87}Sr/^{86}Sr$ has been determined through thermal ionization mass spectrometry (TIMS) techniques. Ca. 20 mg of powder of each sample was weighed in clean PFA Savillex™ vials. Powders were dissolved by adding 4 mL of Milli-Q® (18.2 MΩ resistivity) deionized water to the vials kept closed for 1 h on a hot plate at 120 °C. After 8 min of ultrasonication and 10 min of centrifugation at 4500 rpm in clean tubes, 3.5 mL of the supernatant solutions were transferred to clean PFA vials, then left open on a hot plate at 90 °C until full dryness under a laminar flow hood equipped with HEPA filters. The residues were taken up in 1 mL 2.5 N Suprapur® HCl, ultrasonicated for 8 min, and centrifuged again at 4500 rpm for 10 min in clean tubes. Strontium separation from the matrix was achieved through chromatographic techniques using AG® 50 W X-8 (200 – 400 mesh) BioRad™ ion-exchange resin packed in 2 mL quartz columns. 2.5 M Suprapur® HCl was employed as liquid phase allowing collection of the Sr-bearing solution in clean PFA vials, left open on hot plate at 120 °C under a laminar flow hood for complete evaporation. After nitrification with few drops of 14 M Suprapur® HNO_3, Sr samples were loaded on previously outgassed 99.98 % pure rhenium filaments and finally introduced in a Thermo Scientific™ Triton Plus® solid-source mass spectrometer equipped with nine Faraday cups. Within-run correction was made for possible mass interference on ^{87}Sr by ^{87}Rb, and mass fractionation by normalizing $^{87}Sr/^{86}Sr$ to $^{88}Sr/^{86}Sr = 8.375209$ through an exponential law. The final $^{87}Sr/^{86}Sr$ value is the mean of 150 single runs (15 blocks of 10 cycles each; integration time 16.777 s) at 2σ confidence level following Deines et al. (2003). The NIST SRM 987 international standard measured in the period of samples analysis provided a mean $^{87}Sr/^{86}Sr$ of 0.710243 ± 0.000006 (2σ, $n = 29$); accordingly, the measured $^{87}Sr/^{86}Sr$ values were normalized to the recommended value (0.710248 ± 0.000012; Zhang and Hu, 2020) applying a +0.000005 correction. In the period of chemical processing of the halite samples, the total procedure Sr blank was ca. 100 pg, deemed negligible.

4. Results

4.1. Field observations

In the Coste del Sale area (Fig. 2A), the halite deposit (~2.70 m thick) exhibits an alternation of centimetre-thick white (off-white) and grey layers composed of microcrystalline halite, characteristic of the banded facies. The white layers consist of pure halite crystals, while the grey ones contain halite dispersed within a fine-grained, mud-rich interlayer matrix.

In the Zinga and Verzino areas, salt domes are exposed beneath a Pliocene clay cap (Fig. 2B, G and I). These deposits also include microcrystalline halite from the banded facies, showing similar white–grey alternations, though layer thicknesses vary from centimetres to decimetres (Fig. 2C, H and J).

In addition to the banded facies, the Zinga area hosts a salt dome that includes two different halite facies (Fig. 2G), referred to as the white and transparent facies. Stratigraphically, the white facies is located at the base of the deposit and continues upwards uninterrupted (over ~ 5 m) to the transparent facies. The white facies (Fig. 2E) is characterised by large halite crystals (> 5 cm) displaying alternating milky and clear bands. The milky bands are rich in fluid inclusions, which are visible even during field observation. The overlying transparent facies (not previously described in the literature; Fig. 2F) is composed of similarly large, but distinctly translucent halite crystals. This facies is termed "transparent" due to the translucency of the crystals observed in the field, which appear to have undergone recrystallisation (secondary origin). Sulphate nodules (> 1 cm) are consistently observed across all halite deposits.

Table 1 delineates the main information about the sampling areas, the specific names of the different facies, the texture and name of the sampled crystals, and the previous researches carried out on these crystals over time.

4.2. Petrographic and SEM characterisation of halite facies

4.2.1. Banded facies: Microcrystalline halite

Samples from Coste del Sale, Zinga, and Verzino display very similar features, with well-preserved halite textures. The crystals consist of small halite (< 2 mm in size), occasionally separated and/or covered by thin argillaceous layers (< 2 mm) and scattered clay nodules (up to 0.5 cm). Halite crystals show four distinct patterns: (i) subhedral to euhedral shapes (Fig. 3A), (ii) rafts and flattened plates oriented along the *y*-axis direction [010], which acted as nuclei for (iii) the syntaxial growth of chevrons (Fig. 3A). Clay nodules recognised in these crystals (Fig. 3A C), often incorporate anhydrite minerals and/or amorphous organic materials emitting very green bright UV-epifluorescence (Fig. 3B, C).

Samples from Verzino and Zinga also exhibit additional features, including: (i) randomly oriented crystals, (ii) curved crystal boundaries meeting at triple junctions with angles approaching 120° (Fig. 3D), (iii) clear halite cement (Fig. 3E), (iv) microstructures with polygonal shape and (v) crystals sharply truncated by dissolution.

Transparent filaments and red organic materials, emitting respectively blue and red fluorescence, were also observed throughout the samples (Fig. 3F H).

SEM observations confirmed these optical features and further revealed the microcrystal texture of the halite crystals, and the complex morphology of the amorphous materials trapped within (Fig. 3I) or adjacent to the boundaries crystal. Elemental composition obtained by SEM-EDS indicates that the amorphous substances consist primarily of carbonaceous material (inferred by the high Carbon content) with variable amounts of aluminium (8 37 wt.%), calcium (0.5 3 wt.%), and minor sulphur (< 1 wt.%). In contrast, the halite crystal lattice is composed almost exclusively of sodium and chloride, consistent with its primary mineralogy.

4.2.2. White facies: Bottom-growth crystals

Samples Zi-07 to Zi-09 display large cubic euhedral habit composed of alternating growth bands referred to as milky and clear. The milky bands consist of numerous fluid inclusion (FI) trails that display a chevron shape (chevron fabric; Fig. 4B) and emit bright green UV-epifluorescence (Fig. 4C); these bands are occasionally interrupted by sharp and curved dissolution surfaces. The clear bands are characterised by pure halite crystals and localized microstructures with polygonal shape.

As observed in the microcrystalline of the banded facies, the organic material display various morphologies and fluorescence: transparent filament, green rounded materials and red organic fragments emitting blue, green and red fluorescence, respectively. In these crystals, evidence of dissolution, recrystallisation and fracturing were rarely observed.

SEM observations revealed the presence of abundant FIs and a pervasive disturbance mainly in the milky bands (Fig. 4D, F). Indeed, EDS analyses also reveal a different chemical composition between the bands: clear bands, located away from the milky bands, show only the presence of sodium and chloride, typical of pure halite, whereas milky bands reveal the presence of carbon (C = ~25 wt.%), sodium (Na = ~30 wt.%) and chloride (Cl = ~40 wt.%). Moreover, clear bands adjacent to, and between, milky bands show the same elements recognised in the milky bands but with a lower percentage of carbon (< 21 wt.%).

4.2.3. Transparent facies: Massive crystal

Samples Zi-10 to Zi-14 (Fig. 5A) do not show peculiar petrographic features. They are composed solely of massive crystals made up of translucent and opaque halite. The translucent halite exhibits widespread evidence of intergranular voids and abundant FI trails (Fig. 5B D), whereas the opaque halite lacks observable petrographic characteristics due to its opacity, which obscures all features.

Transparent filaments and rounded red organic materials, emitting blue and red fluorescence, respectively, were observed throughout the samples.

SEM observations confirm the petrographic features identified in the translucent portions of the crystal, while also providing additional information on the opaque areas, which are not visible under optical microscopy. These areas show pagoda halite crystals (crystals with pyramidal or conical form, with progressively smaller layers as they extend upward; Fig. 5E) and reticulate ridge halite on the surface (see Southgate, 1982). Individual cornet-shaped hoppers have ridges radiating at right angles from their corners. Pagoda crystals are smaller than the centrally located hopper and show a successive decrease in size with increasing distance along the ridge. Each ridge consists of several horizontally stacked halite corner growths. Thin ridges radiate from hopper corners, thin, with increasing length, and either taper to a point or abut without distortions occurring. Several pagoda-type hopper regrowth was characterised by curved sides that truncate hopper growth planes, implying partial hopper dissolution. Semi-quantitative analyses on pure halite crystals show the presence of sodium, chloride, and potassium. Elemental composition obtained by SEM-EDS indicates that both translucent and opaque halite are constituted by sodium (Na = ~29.5 wt.%), chloride (Cl = ~63.4 wt.%), and potassium (K = ~7.1 wt.%).

4.3. Fluid inclusion petrography

Both primary and secondary FIs are observed in all samples through optical and scanning electron microscopy. Primary FIs run parallel to the faster active growth faces (100) and reflect the cubic crystallography of the host mineral. FIs are also distributed in the crystal corners and sometimes show chevron fabric, which is visible mainly in Zi-07 to Z-14 samples. Three types of primary FIs were identified (Figs. 6 and 7; Table 2):

(1) Type 1 monophase liquid-rich inclusions have tabular or negative crystal shapes (Fig. 7B). They range in size from 5 μm to 55 μm (avg. 30 μm) in microcrystalline halite, from

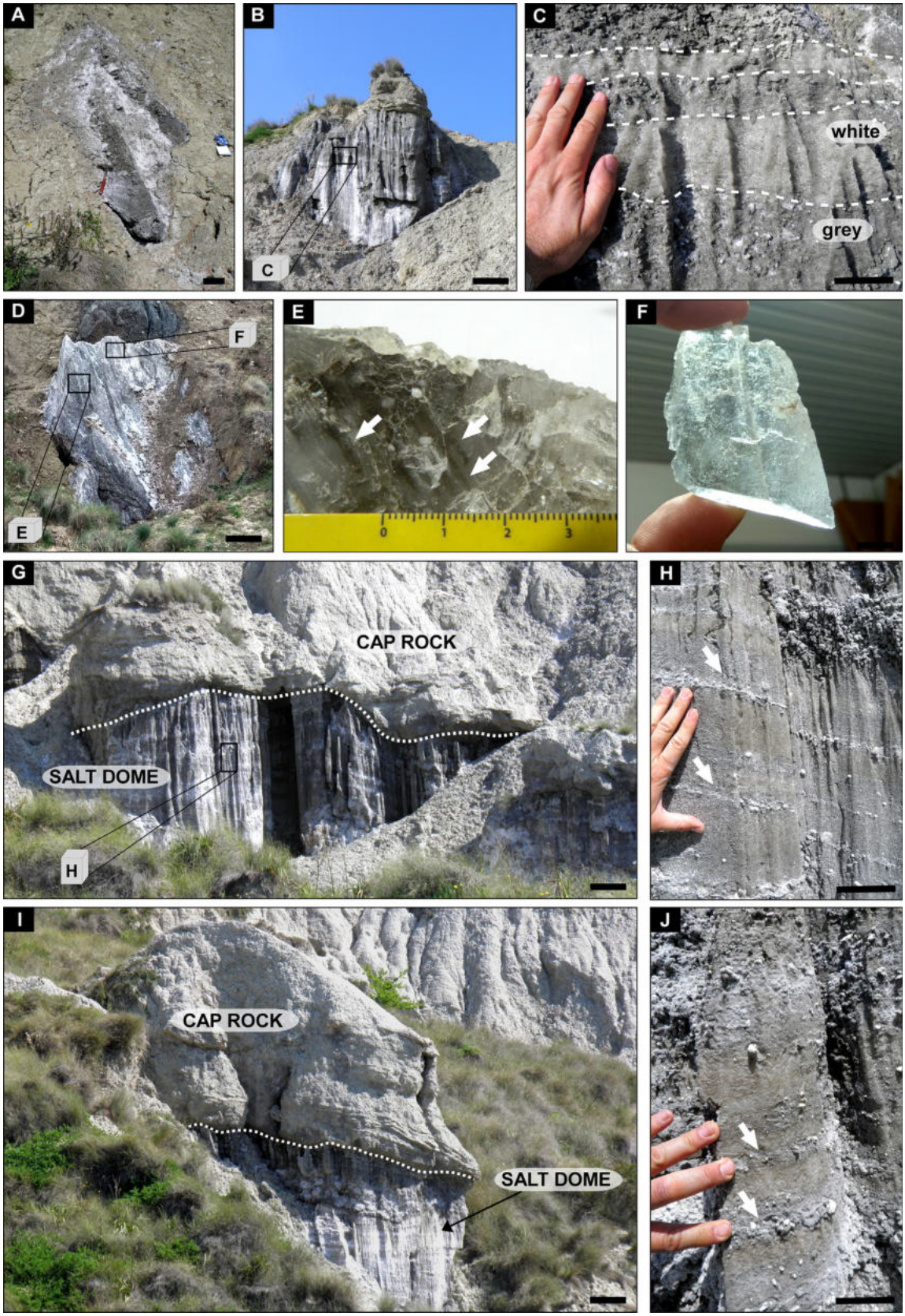

Fig. 2. Halite deposits located in the Crotone Basin showing the three different facies. (A) Individual halite deposit (banded facies) outcropping in the Coste del Sale (scale bar = 20 cm). (B) First halite salt dome (banded facies) in the Zinga area, and (C) detail showing white (off-white) and grey bands, highlighted with dotted white lines (scale bar = 40 cm). (D) Second halite salt dome in the Zinga area (scale bar = 20 cm) and detail of halite crystals sampled from white (E) and transparent facies (F); white arrows indicate grey bands devoid of fluid inclusions. (G) and (I) Two main salt domes (scale bars = 20 cm) recognised in the Verzino area showing cap rock above the halite deposits (spotted white line) and magnification (H and J) showing dark layers (white arrows) interbedded by anhydrite and clay intervals (scale bars = 4 cm).

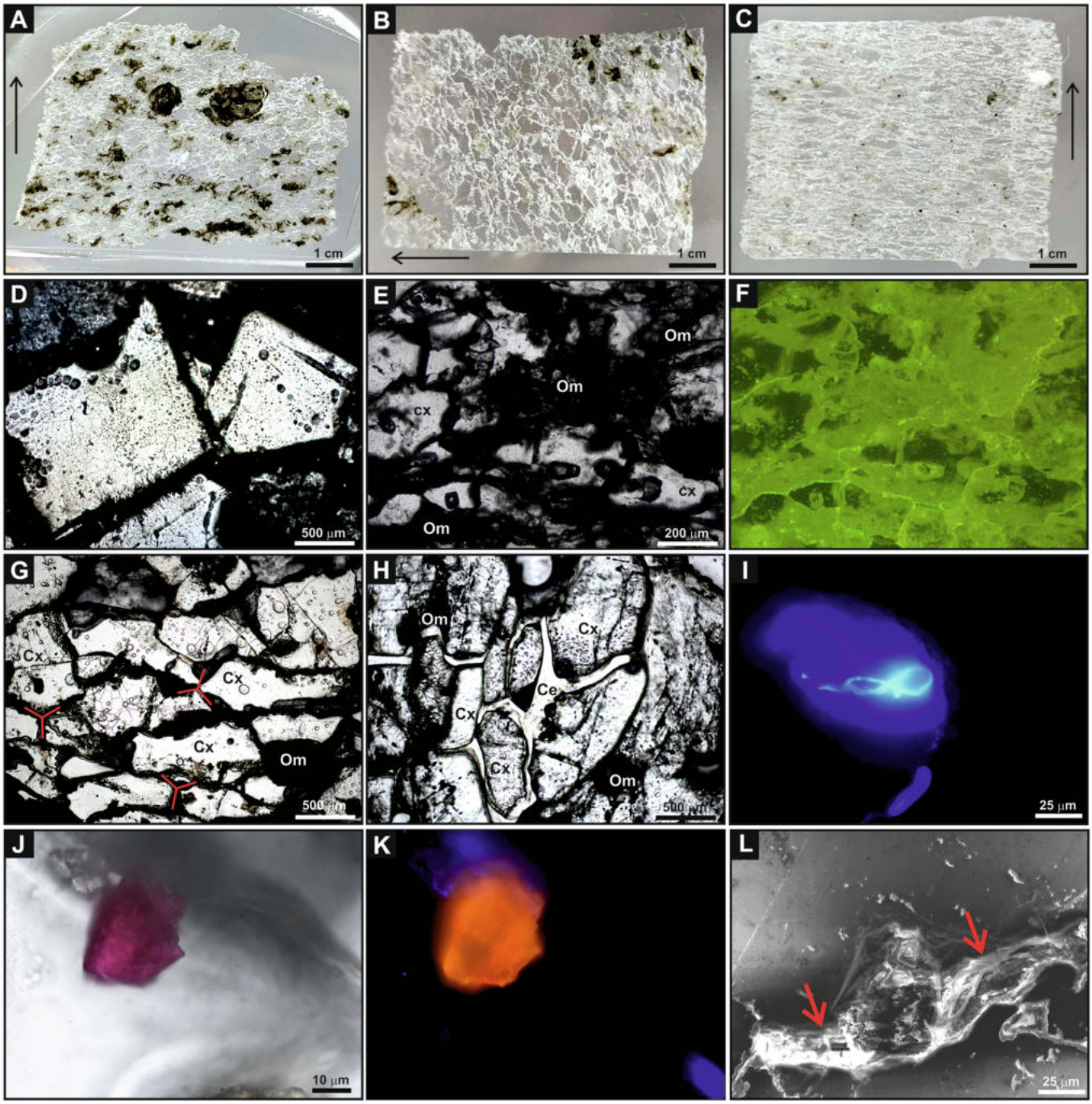

Fig. 3. Main petrographic features of microcrystalline halite samples: CS-01 (A), Zi-01 (B) and Ve-01 (C), observed in thin sections through optical microscopy (D H, J), UV-epifluorescence (I and K) and SEM (L); black arrows indicate the growth direction. (D) Sample from Coste del Sale showing subhedral and syntaxial growth of chevrons crystals. (E) Amorphous organic materials (Om), that separate and cover halite crystals (Cx), emitting bright fluorescence (F). (G) Sample from Zinga displaying curved crystal boundaries meeting at triple junctions with angles approaching 120° (red lines). (H) Sample from Verzio showing clear halite cement (Ce). (I K) Transparent filaments and red organic materials, emitting respectively blue and red fluorescence. (L) Amorphous materials between halite crystals (red arrows).

5 µm to 145 µm (avg. 65 µm) in bottom-growth and from 5 µm to 80 µm (avg. ~ 35 µm) in massive crystals. A total of 362 Type 1 FIs have been studied.

(2) Type 2 are two-phase liquid-rich (L > V) inclusions displaying mainly tabular, irregular and negative crystal shapes (Fig. 7B). They range in size from 5 µm to 150 µm (avg. 60 µm) in microcrystalline halite, from 8 µm to 200 µm (avg. 90 µm) in bottom-growth crystals and from 5 µm to 400 µm (avg. 100 µm) in massive crystals. The degree of fill [$F = V_L/V_{TOT}$, where F is the volumetric proportion of liquid (V_L) relative to the total volume (V_{TOT}) of the inclusion] ranges between 0.70 and 0.98 (avg. 0.87). A total of 420 Type 2 FIs have been observed.

(3) Type 3 are multiphase inclusions (L ± V ± S ± OM) containing mainly a liquid phase with subordinate amounts of vapour, organic material and/or solid phases. They show irregular

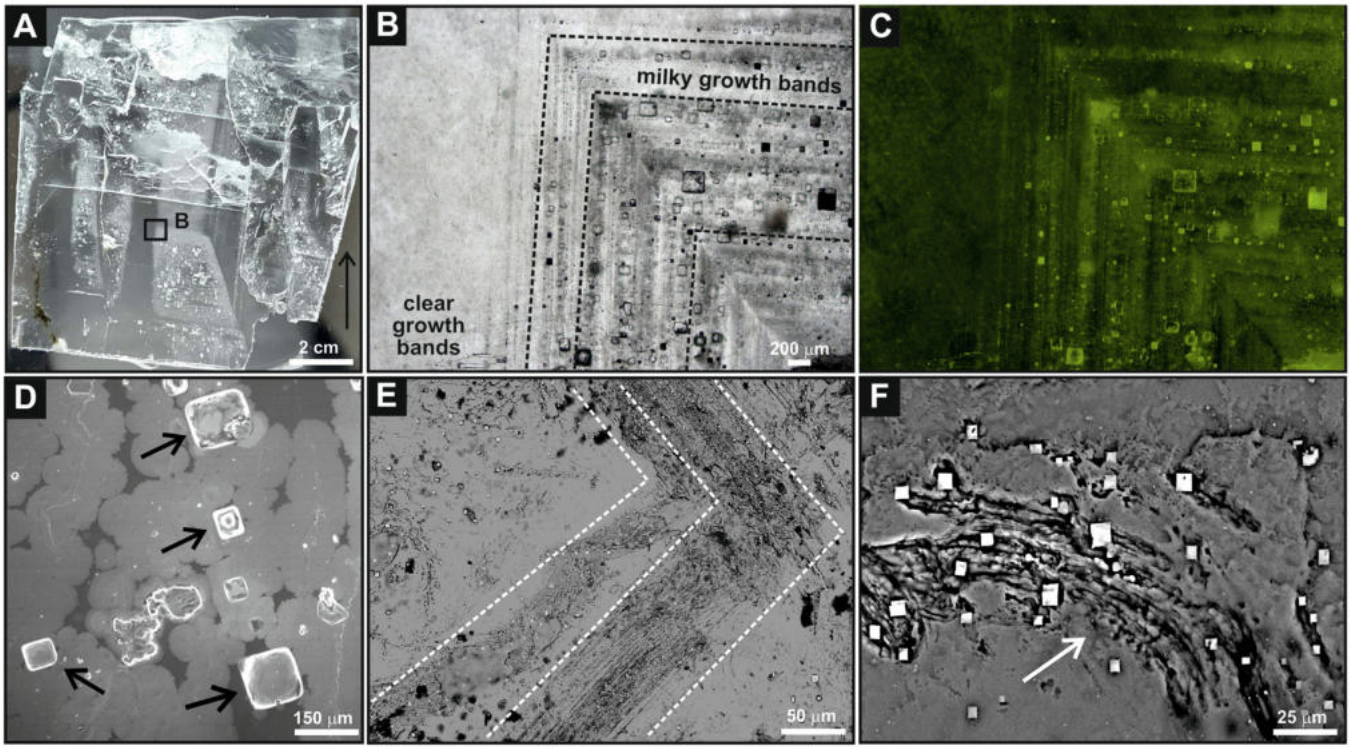

Fig. 4. (A) Main petrographic features of Zi-07 sample (bottom-growth crystal) observed in thin sections through transmitted light (B), UV-epifluorescence (C) and SEM (D–F); black arrow indicates the growth direction. (B) and (C) Enlargement of a detail showing the alternating milky (white dotted lines) and clear growth bands. Note the UV-epifluorescence in correspondence of milky bands (C). (D) Detail of fluid inclusions observed in the milky band. (E) FI trails in correspondence of milky bands. (F) Detail of the irregular crystal lattice of the milky bands (white arrow), probably due to the presence of organic remains.

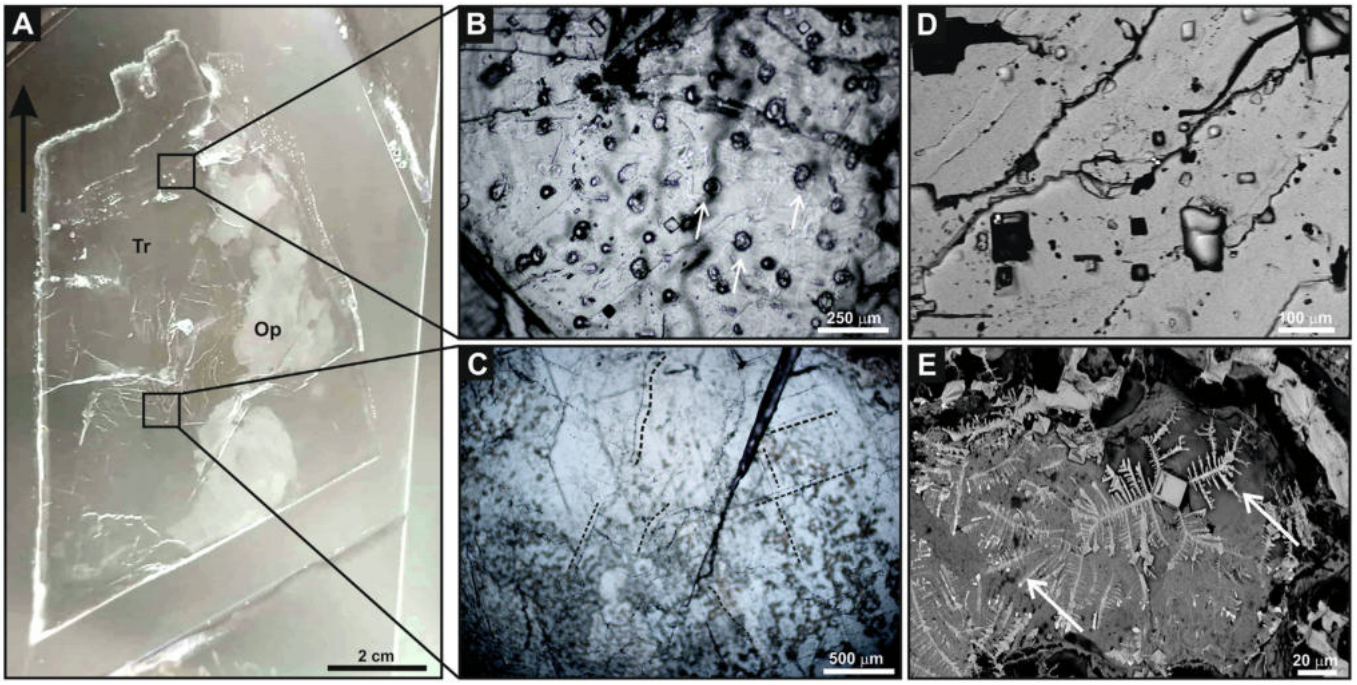

Fig. 5. (A) Main petrographic features of Zi-14 sample (massive crystal) observed in thin sections showing translucent (Tr) and opaque (Op) halite; black arrow indicates the growth direction. (B) Translucent halite shows intergranular voids (white arrows) and (C) linear and irregular FI trails (black dotted lines). (D) and (E) show the surface of the translucent and opaque parts of the sample, respectively. In the translucent area, fractures and fluid inclusions are clearly visible, whereas the opaque part displays characteristic pagoda crystal structures (white arrows).

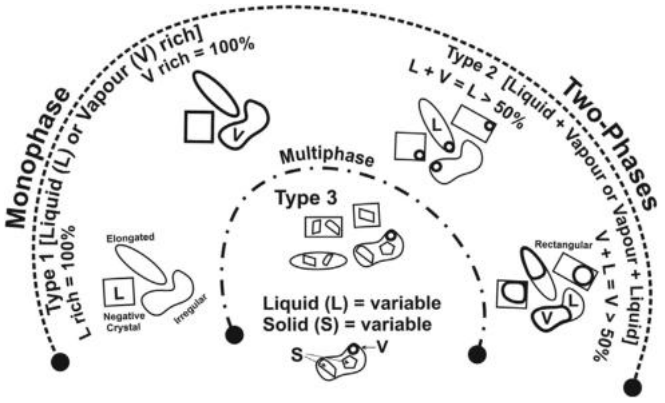

Fig. 6. Schematic classification showing FI phases of primary inclusions recognised in halite crystals. Phases present at room temperature and various morphologies observed are arranged with respect to the amount of liquid (L) and/or vapour (V) as well as solid (S) and organic material (OM) trapped within the inclusions.

and negative crystal shapes (Fig. 7C–I) and range in size from 10 μm to 155 μm (avg. 80 μm) in microcrystalline halite, from 10 μm to 350 μm (avg. 125 μm) in bottom-growth and from 10 μm to 400 μm (avg. 230 μm) in massive crystals. Massive crystals exhibit a higher number of Type 3 FIs compared to microcrystalline and bottom-growth crystals. A total of 189 Type 3 FIs have been observed.

Trapped organic material in Type 3 FIs display colours ranging from brown/orange to colourless, with morphologies ranging from rounded to irregular (< 10 μm in size). These inclusions occur in clusters and are commonly found near the FI corners or in their core. They emit bright blue or red UV-epifluorescence. Well-preserved, rounded, orange organic materials are also mainly observed in the bottom-growth crystal. Three main types of organic materials trapped within fluid inclusions were recognised: (i) rounded red/orange (Fig. 7C), (ii) amorphous (Fig. 7C, D and G) and (iii) black amorphous (Fig. 7F). Red/orange and amorphous materials are recognised in all three types of facies, whereas black substances were predominantly found in the massive crystals.

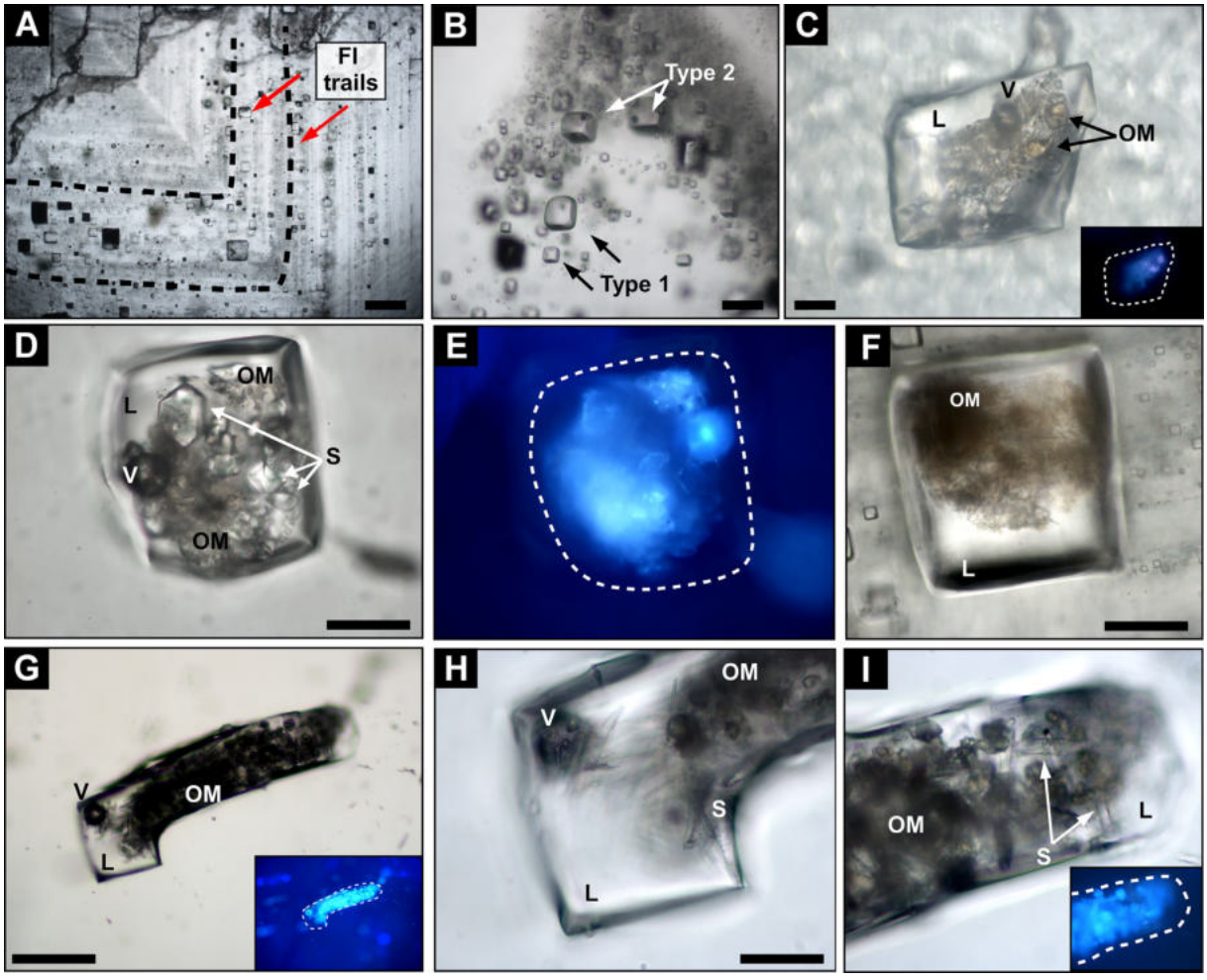

Fig. 7. FIs observed in the banded (A, B), white (C, F) and transparent (G–I) facies through transmitted and UV-epifluorescence light (white dotted line). (A) Type 1 and Type 2 FI trails defying chevron fabric; note the orientation and septum that bisects the chevron (scale bar = 100 μm). (B) Group of Type 1 and Type 2 FIs showing negative crystal shapes (scale bar = 50 μm). (C) Individual Type 3 FI showing organic material emitting fluorescence (scale bar = 50 μm). (D–F) Type 3 FIs black amorphous materials showing green fluorescence (scale bar = 100 μm). (G) Elongated FI trapping solids and organic material (scale bar = 20 μm) and magnification (H and I) of its left and right rims; OM emitting bright blue fluorescence (scale bar = 10 μm). OM = organic material; V = vapour; L = liquid; S = solid.

Table 2
Summary list of primary FIs characteristics observed in banded, white and transparent facies.

Halite facies	Crystals	FI types	FI shapes	FI sizes (μm)
Banded	Microcrystalline	Type 1	Tabular and negative crystal	5–55 (avg. 30)
		Type 2	Tabular, irregular and negative crystal	5–110 (avg. 50)
		Type 3	Irregular and negative crystal	10–155 (avg. 80)
White	Macrocrystalline (Bottom-growth)	Type 1	Tabular and negative crystal	5–145 (avg. 65)
		Type 2	Tabular, irregular and negative crystal	8–200 (avg. 90)
		Type 3	Irregular and negative crystal	10–350 (avg. 125)
Transparent	Macrocrystalline (Massive)	Type 1	Tabular and negative crystal	5–80 (avg. 35)
		Type 2	Tabular, irregular and negative crystal	5–400 (avg. 100)
		Type 3	Irregular and negative crystal	10–400 (avg. 230)

Solids hosted within the inclusions (Fig. 7D, H, I) are colourless and range in size from 5 μm to 50 μm. They show various shapes: prismatic, rounded, tabular, elongated, and acicular. Semi-quantitative analyses carried out on solids trapped in type 3 FIs show the presence of:

(a) gypsum (rounded or prismatic habit), bassanite (acicular or elongated-prismatic habit), and anhydrite (tabular, lamellar or elongated shapes) crystals. Gypsum and anhydrite solids were recognised in all samples, whereas bassanite was only identified in bottom-growth crystal;
(b) amorphous organic material consisting of carbonaceous remains.

Primary FIs are abundant and well-preserved, particularly in the milky chevron bands of the bottom-growth crystals. Indeed, within a single milky band, "high frequency" fluid inclusion bands are present. A typical milky band contains between 10 and 20 of these high-frequency bands. 56 milky bands were counted in only 2 – 5 cm of an individual crystal. Each of these high-frequency bands is considered an individual fluid inclusion assemblage (Goldstein and Reynolds, 1994; Benison and Goldstein, 1999), meaning that all fluid inclusions along each band formed at the same time.

Secondary FIs are distributed in groups or linear trails along annealed microfractures and cleavage planes. Sometimes, they cross-cut chevron and corner growth bands; however, they are generally less abundant than primary inclusions. Scattered secondary FIs are affected by re-equilibration phenomena, such as stretching, leaking and necking-down processes (Fig. 8), which involve dissolution and re-precipitation of the host phase to reduce the surface area, producing many smaller inclusions from the original larger inclusion (see Larson et al., 1973; Bodnar and Bethke, 1984; Bakker and Jansen, 1990; Hall et al., 1993; Vityk et al., 2000). Some inclusions show a dark appearance, indicative of decrepitation phenomena (fluid loss). Two types of secondary FIs have been recognised: Type 1 (monophase, liquid or vapour) and Type 2 (two-phase, liquid-rich or vapour-rich). Both types display irregular to negative crystal shapes and range in size from 2 μm to 30 μm.

4.4. Fluid inclusion microthermometry

Microthermometric data are recorded on 380 fluid inclusions hosted in halite crystals of the banded (n = 180), white (n = 135) and transparent (n = 65) facies to obtain the temperature of first melting (T_{FM} – chemical composition of the brine) and Temperature of homogenization (T_H – temperature of the origin brine) (Table 3).

- In microcrystalline halite samples from Costa del Sale (CS-01, CS-03, CS-04 samples), analyses were carried out on 40 Type 1 and 25 Type 2 FIs. Type 1 inclusions show mainly negative crystal shapes and range in size from 16 μm to 30 μm (avg. 20 μm). T_{FM} is recorded at ~ –35 °C (H_2O-NaCl-$MgCl_2$ salt system) and T_H at +32 °C. Type 2 inclusions display mainly elongated shapes, a degree of fill between ~ 0.70 and ~ 0.94, and range in size from 40 μm to 72 μm (avg. 63 μm). T_{FM} is recorded at ~ –36 °C (H_2O-NaCl-$MgCl_2$ salt system) and T_H at +32 °C.
- In microcrystalline halite samples from Zinga (Zi-01, Zi-03, Zi-04), analysis was carried out on 22 Type 1 and 30 Type 2 FIs. Type 1 inclusions show negative crystal shape and range in size from 18.4 μm to 50 μm (avg. 28 μm). T_{FM} is recorded at –35 °C ± 1 °C (H_2O-NaCl-$MgCl_2$ salt system) and T_H at +20 °C. Type 2 inclusions show elongated and negative crystal shapes, a degree of fill between ~ 0.75 and ~ 0.97 and range in size from 20 μm to 140 μm (avg. 66 μm). T_{FM} is recorded at –35 °C (H_2O-NaCl-$MgCl_2$ salt system) and T_H at +34 °C.
- In microcrystalline halite samples from Verzino (Ve-01, Ve-03 and Ve-05 samples), analysis was carried out on 25 Type 1 and 38 Type 2 FIs. Type 1 inclusions show negative crystal shape and range in size from 10 μm to 17 μm (avg. 23 μm); 10 inclusions show T_{FM} at –23 °C (H_2O-NaCl-KCl salt system) and T_H at +44 °C, while 15 inclusions have T_{FM} at –34 °C (H_2O-$MgCl_2$ or H_2O-NaCl-$MgCl_2$ salt system) and T_H at +33.5 °C. Type 2 inclusions show negative crystal shape, degree of fill between ~ 0.93 and ~ 0.95 and range in size from 14 μm to 120 μm (avg. 43 μm); 18 inclusions show T_{FM} between –24 °C (H_2O-NaCl-KCl salt system) and T_H between +40 °C and +44 °C, while 20 inclusions have T_{FM} at –35 °C (H_2O-$MgCl_2$ salt system) and T_H at +35°C.
- In samples from the bottom-growth crystals of Zinga (Zi-07 and Zi-09 samples), analysis was carried out on 55 Type 1 and 80 Type 2 FIs located within the milky bands. They occur in linear trails, show negative crystal shapes and range in size from ~ 10 μm to ~ 200 μm (avg. 100 μm); Type 2 FIs show a degree of fill between ~ 0.74 and ~ 0.98 (avg. ~ 0.93). T_{FM} is recorded in 20 Type 1 and 33 Type 2 FIs and occurred at –35 °C ± 1 °C (avg. –34 °C; H_2O-NaCl-$MgCl_2$ salt system) in both Types. T_H is recorded from FIs forming the high-frequency growth bands; they show a decrease in values from +44 °C, obtained on the base, to +50 °C on the top of the chevron.

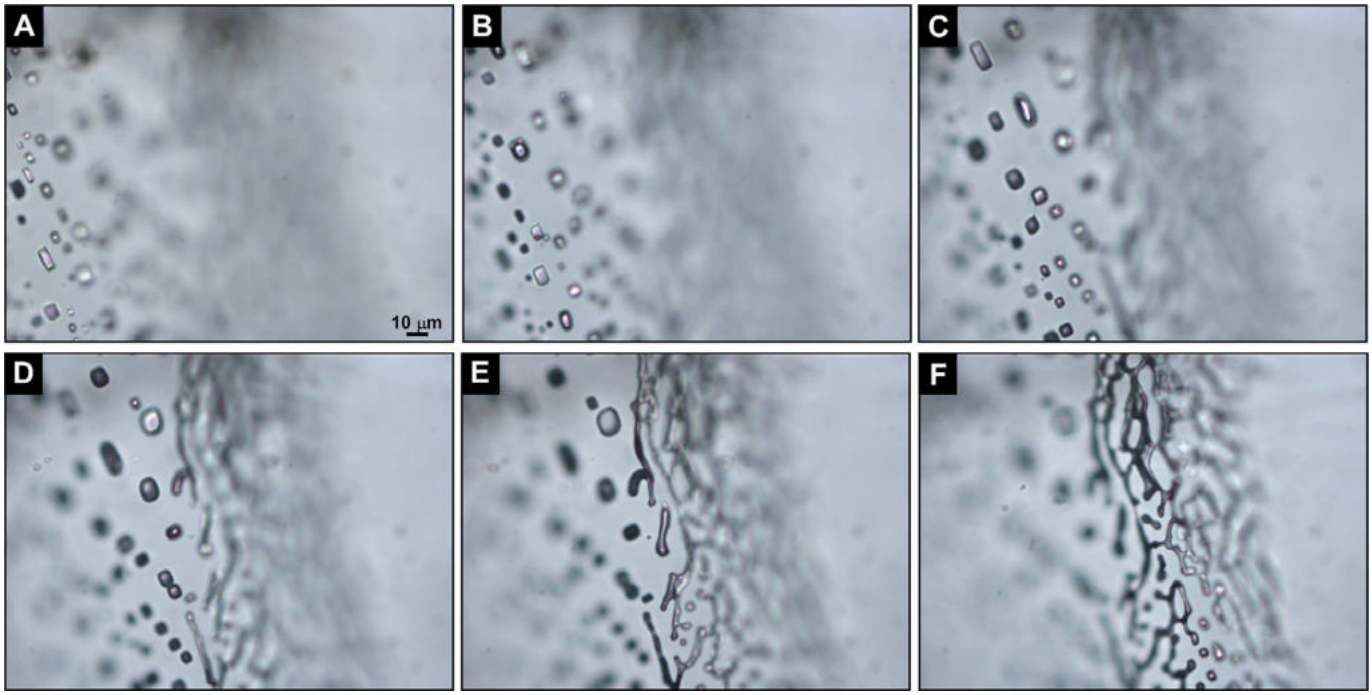

Fig. 8. Necking-down process in halite crystal, observed from bottom to top, using different plane of focus. Pictures from (A) to (D) show smaller inclusions from the original larger inclusion still visible in (E) and (F) photos. The scale bar shown in panel (A) applies to all images.

Table 3
Summary of microthermometric data for the analysed halite samples, including facies, fluid inclusion (FI) types, number of measurements (*n*), inclusion sizes, temperature of first melting (T_{FM}), and homogenization temperature (T_H).

Samples	Facies	FI types	*n*	FI sizes (μm)	T_{FM} (°C)	T_H (°C)
CS-01	Banded	Type 1	40	16 – 30	–35	+32
CS-03				(avg. 30)		
CS-04		Type 2	25	40 – 472 (avg. 63)	–36	+32
Zi-01	Banded	Type 1	22	18.4 – 50	–34 to –36	+20
Zi-03				(avg. 28)	(avg. –35)	
Zi-05		Type 2	30	20 – 140	–35	+34
				(avg. 66)		
Ve-01	Banded	Type 1	10	10 – 17	–23	+44
Ve-03			15	(avg. 23)	–34	+33.5
Ve-05		Type 2	18	14 – 120 (avg. 43)	–24	+40
			29		–35	+35
Zi-07	White	Type 1	55	10 – 130	–34 to –36	+44 to +50
Zi-09				(avg. 45)	(avg. –35)	(avg. 45)
		Type 2	80	10 – 200		
				(avg. 125)		
Zi-10	Transparent	Type 1	25	8 – 50	–32 to –33	+18 to +22
Zi-12				(avg. 25)		(avg. 20)
Zi-14		Type 2	40	10 – 50		
				(avg. 32)		

- n samples from the massive crystals of Zinga (Zi-10, Zi-12 and Zi-14 samples), analysis was carried out on 25 Type 1 and 40 Type 2 FIs displaying elongated, tabular or negative crystal shape and range in size from 8 μm to 50 μm (avg. 25 μm); Type 2 FIs have a degree of fill between 0.90 and ~ 0.98 (avg. ~ 0.96). In both FI types, T_{FM} is documented at –33 °C ± 1 °C (H_2O-$MgCl_2$ salt system), while T_H is recorded from +18 °C to +22 °C (avg. 20 °C).

4.5. Chemical characterisation with Raman spectroscopy

In bottom-growth crystal, Raman analysis was conducted on (i) portions of the crystal devoid of FI trails, (ii) crystal enriched in FI trails, (iii) organic materials trapped in Type 3 FIs and (iv) Type 1 FIs. In details, the following spectral signatures were observed:

(i) six prominent absorption bands around 358, 1337, 1582, 2678, 2884 and 2940 cm^{-1} (Fig. 9A) in crystal devoid of FI trails;
(ii) peaks at 358 cm^{-1}, a significant bump in the region between 1200 cm^{-1} and 1600 cm^{-1}, and peaks at 2250, 2686, 2930 cm^{-1} (Fig. 9B) in crystal enriched in FI trails;
(iii) peaks around 263, 1149, 1614, and 2900 cm^{-1} (Fig. 9C) and around 1150 – 1570 cm^{-1} and 1500 – 1550 cm^{-1} in dark FIs;
(iv) a bump between 500 and 2000 cm^{-1} and a peak at 2930 cm^{-1} (Fig. 9D) in liquid FIs.

Moreover, solid crystals trapped within Type 3 inclusions have been identified as anhydrite ($CaSO_4$), gypsum ($CaSO_4{\cdot}2H_2O$) and halite (NaCl).

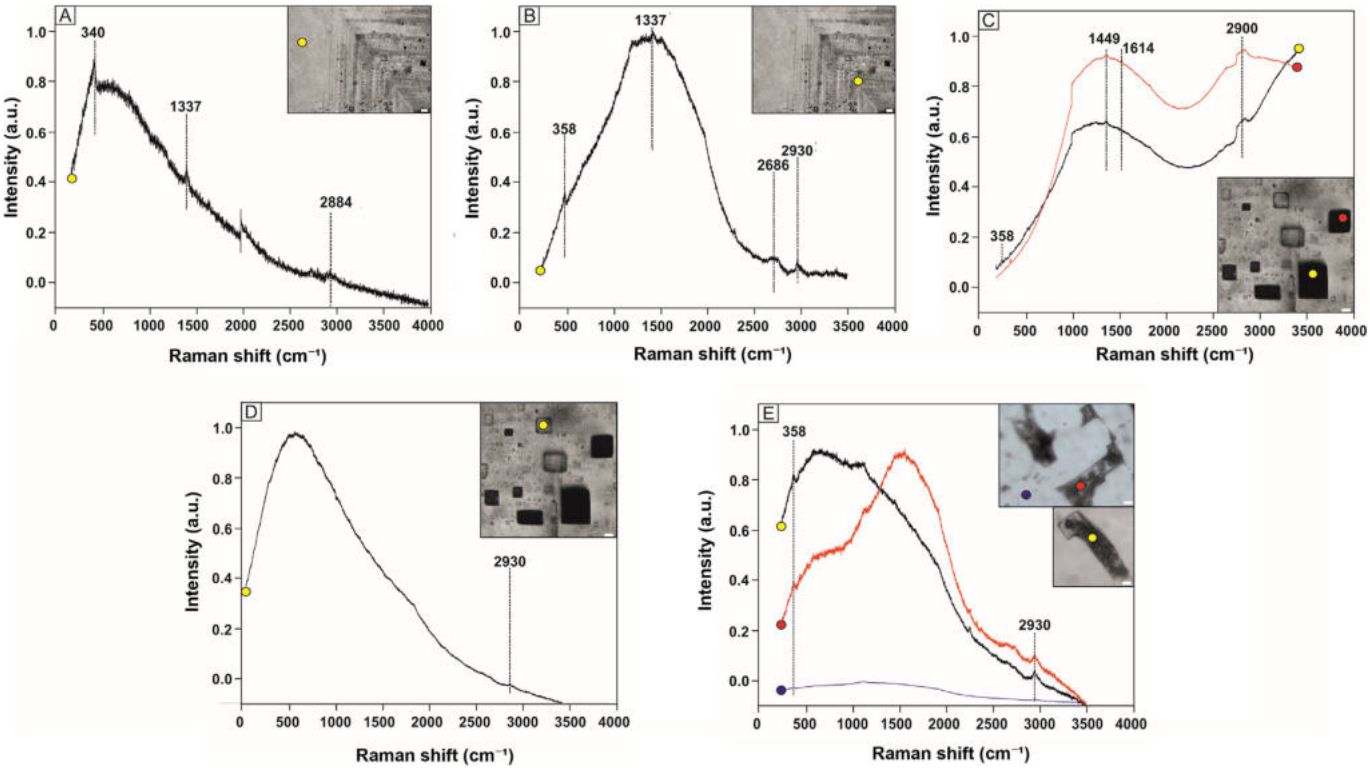

Fig. 9. Raman spectra (range between 0 and 4000 cm^{-1}) collected from different areas of bottom-growth (A to E) and massive (D) crystals. Red, yellow, and blue dots mark analysis points shown in panels (A-E), while black, red, and blue lines display the corresponding spectra. Note that the Raman spectra showing bumps at the peaks around 1340 $cm^{-1}$and 1600 cm^{-1} are related to the D- and G-Bands, which are typical of the organic material. The scale bar in the pictures is 200 μm (A, B and E) and 50 μm (C and F). The *x*-axis represents the Raman shift (in cm^{-1}), and the *y*-axis indicates relative normalized intensity (a.u. = arbitrary units).

Regarding massive crystal, analyses were conducted on Type 3 FIs and pure halite crystals. Type 3 FIs have showed two bumps (Fig. 9E): (i) in the region between 500 and 1200 cm^{-1}, and (ii) between 1500 and 2000 cm^{-1}, with main peaks at 358 and 2930 cm^{-1}, while analyses carried out on pure halite crystals showed the same peaks recognised in Type 3 inclusions but with significantly lower intensity.

4.6. 3D Image analysis through synchrotron radiation X-ray computed microtomography (SR X-ray μCT)

The distribution, size, and morphology of fluid inclusions were assessed using Synchrotron Radiation X-ray Computed Microtomography (SR X-ray μCT). Both samples, Zi-08 and Zi-14, exhibited similar morphologies of primary fluid inclusions, however they differ significantly in terms of abundance and spatial arrangement.

In bottom-growth crystals, Type 1 inclusions, primarily associated with milky growth bands, are the most abundant (Fig. 10A), followed in frequency by Type 2 and Type 3 inclusions (Fig. 10 B–C). Conversely, in massive crystals, the relative abundance is inverted, with Type 3 inclusions being the most common, followed by Type 2 and Type 1 inclusions.

Throughout the entire volume of the two samples, Type 1 inclusions showed mainly tabular and negative crystal shapes, regardless of their size. Type 2 inclusions displayed negative crystal shapes for those smaller than 0.2 mm and irregular shapes for those larger than 0.2 mm. In contrast, Type 3 inclusions were consistently irregular, regardless of size, reflecting their complex genesis.

As previously mentioned, the Type 3 FIs can contain crystalline solids and/or organic materials. Although the detection of organic matter via SR X-ray μCT is limited due to its low density and poor contrast, solid inclusions (*e.g.*, halite, gypsum, anhydrite) are readily visible and characterised by sharp, well-defined edges. In terms of internal structure and FI distribution, Zi-08 displays a well-developed chevron fabric, with Type 1 inclusions densely concentrated along the milky bands, and largely absent or sparse in the intervening clear bands (Fig. 11A).

In contrast, Zi-14 did not display a chevron structure; however, well-defined trails of primary fluid inclusions were still clearly visible, although they appeared more irregularly distributed throughout the crystal volume. The sample also exhibited an extensive network of fractures, some of which host secondary inclusions. In several cases, these secondary inclusions exhibited necking-down phenomena (Fig. 11B). The co-occurrence of primary and secondary inclusions in Zi-14 suggests a more complex diagenetic history compared to growth-zoned fabric observed in Zi-08.

4.7. $^{87}Sr/^{86}Sr$ isotopic signature

Five samples from different crystals were used for isotopic analysis. Microcrystalline samples displayed $^{87}Sr/^{86}Sr$ values of 0.708 950 ± 0.000006 (2 s.e.), 0.708918 ± 0.000007 (2 s.e.) and 0.70892 5 ± 0.000008 (2 s.e.); Zi-07 sample from the bottom-growth crystals show $^{87}Sr/^{86}Sr$ of 0.708934 ± 0.000007 (2 s.e.) and Zi-14 sample from the massive crystal show $^{87}Sr/^{86}Sr$ of 0.709050 ± 0.000007 (2 s.e.).

Plotting these values on the global ocean field and considering the development of the Sr isotope curve in the Mediterranean Sea during the MSC (*see* Roveri et al., 2014), the values fall between 5.60 Ma and 5.55 Ma (Fig. 12).

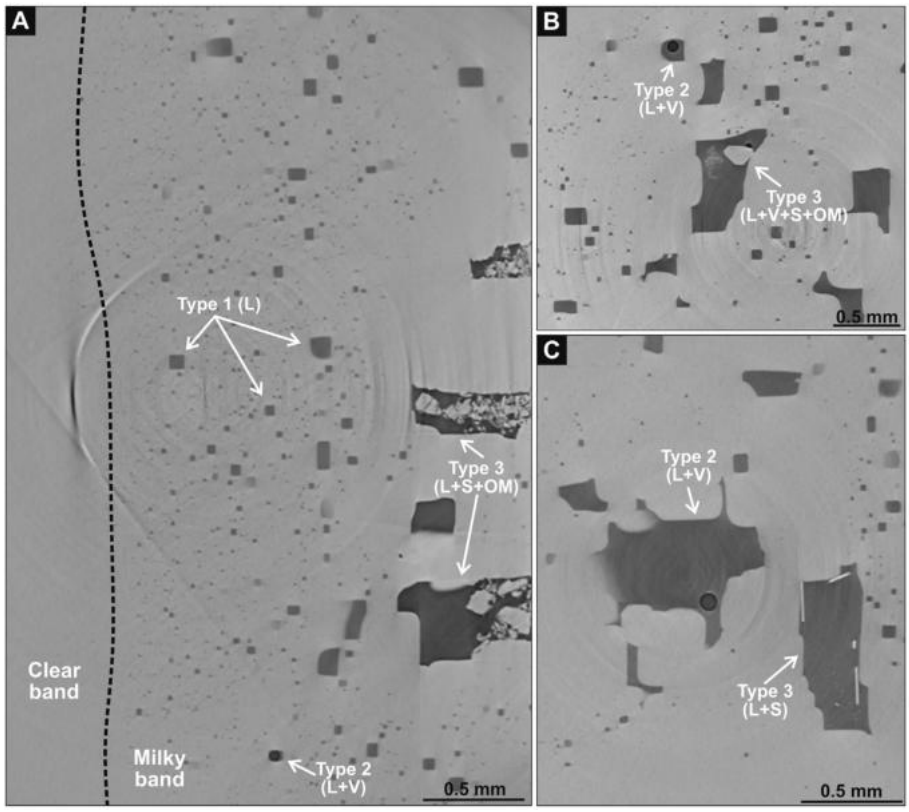

Fig. 10. Different types of FIs observed in slices of the Zi-08 sample. (A) A portion of crystal showing clear and milky bands; milky band is enriched in Type 1 FIs with sporadic Type 2 and Type 3. (B) Irregular Type 3 inclusion showing a big solid crystal and scattered organic material trapped within; the orientation of the samples does not allow observation of the solids trapped among the other Type 3 inclusions. (C) Very large Type 2 and Type 3 inclusions with anhydrite crystals. OM = organic material; V = vapour; L = liquid; S = solid.

5. Discussion

5.1. Facies interpretation

5.1.1. Microcrystalline halite from the banded facies

Halite deposits belonging to the banded facies, recognised in all three investigated areas (Coste del Sale, Zinga and Verzino), consist of alternations of white (pure halite), known as "cumulate halite" (Hovorka, 1987; Benison and Goldstein, 1999; Goldstein, 2001; Kiro et al., 2016), and grey layers, made up of cumulate halite crystals immersed in thin mud-rich layers. Although primary sedimentary structures are largely obliterated, the occurrence mudstone/siltstone layers suggest repeated episodes of flooding and dilution of the salt basin by undersaturated, muddy waters.

In details, in the banded facies, recognised in the Crotone Basin, the eutectic point measured during microthermometric analyses suggested a comparable H_2O-NaCl-$MgCl_2$ brine composition for all samples, except for Ve-01 and Ve-05 samples in which K^+ becomes the dominant cation (H_2O-NaCl-KCl) (Fig. 13). The Mg-dominant compositions agree with the conditions of extreme supersaturation previously assumed for the original brine. As reported by Warren (2006), in a closed system, as seawater concentrates, the first mineral to precipitate is Calcite/Aragonite in a salinity range between 40 ‰ and 60 ‰. As the brine continues to concentrate and approaches water salinity of 130 ‰ – 160 ‰ (4 – 5 times the concentration of seawater), gypsum precipitates from penesaline waters. Finally, at 10 – 12 times the original concentration (salinity range between 340 ‰ – 360 ‰), halite begins to precipitate from supersaline marine waters. At later stages, when seawater is concentrated more than 70 – 90 times, K-Mg salts crystallise (Warren, 2006). The steady increase in total dissolved solids (TDS) during the ongoing evaporation of seawater produces two types of brine: Na-Cl brines and Mg-Cl-SO_4 brines. Na-Cl brines dominate between 35 ‰ and 330 ‰, but at higher salinities, Mg-Cl-SO_4 brines become prevalent due to the progressive removal of Na^+ by halite precipitation. Initially, magnesium dominates, but as $MgSO_4$ salts begin to crystallise, K^+ takes its place. Cl^- remains the dominant anion throughout.

This evaporative sequence is consistent with the chemical evolution models proposed by Bąbel and Schreiber (2014), who emphasize that the relative abundances of Mg^{2+} and K^+ in the residual brines are highly sensitive to both the extent of halite precipitation and the degree of brine recycling or isolation. In particular, the authors suggested that the late-stage enrichment in potassium often signals prolonged evaporation under hydrologically restricted conditions, with limited inflow and high residence times. Moreover, they underline that Mg-rich brines, especially those enriched in $MgCl_2$, are a hallmark of advanced evaporative concentration, and their persistence in the inclusion record reflects minimal dilution or flushing by meteoric or marine waters after halite deposition. These observations further support the interpretation that the sampled halite record an advanced stage of evaporation, with Ve-01 and Ve-05 potentially capturing a transitional geochemical phase between Mg- and K- dominance in the residual brine.

The average temperature value of the brine, obtained through microthermometric analyses, is about ±34 °C (between 20 °C and 45 °C). These water temperatures might seem very high, however, Lugli and Lowenstein (1997) obtained similar homogenization temperatures for primary fluid inclusions in halite hoppers crystals

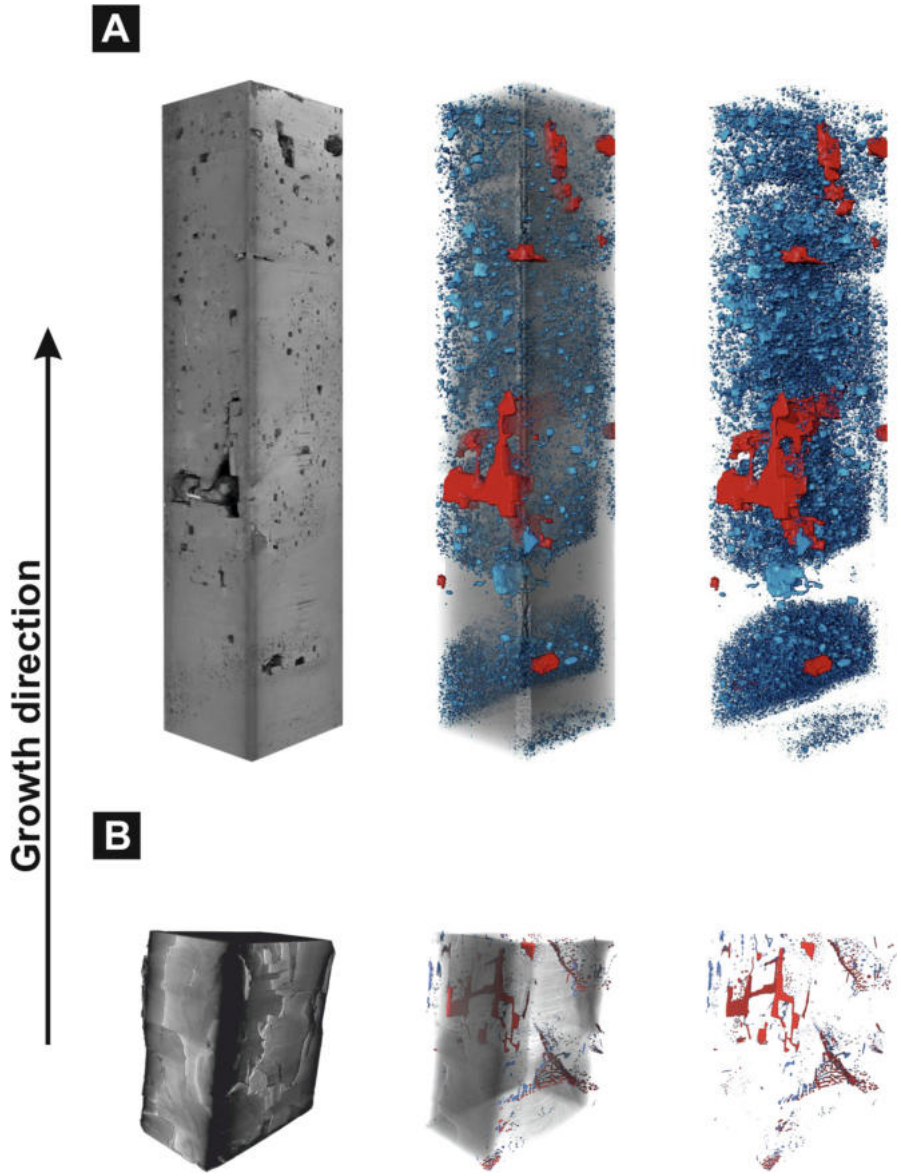

Fig. 11. 3D rendering of Zi-08 (A) and Zi-14 (B) samples in progressive transparency to highlight the distribution and quantity of primary (blue colour) and secondary inclusions and fractures (in red colour).

taken from a complete mud-halite-mud cycle of Unit C of Realmonte mine (Sicily). They concluded that the Realmonte salt deposit formed by precipitation from a homogeneous column of shallow water. Similar data were obtained by Roberts and Spencer (1995) and Lowenstein et al. (1998) who measured temperatures in the range 30 – 40 °C in halite fluid inclusions from salted lakes in the Death Valley, California. The temperature reported in this paper are also in agreement with more recent results obtained by Rigaudier et al. (2011) and Galamay et al. (2023) from microthermometric studies carried out on Messinian halite from Realmonte mine (Sicily) and Messinian Salt in the Tuz Gölü Basin (Turkey), respectively. They recognised a variable range of brine temperature from 21.8 °C to 41.5 °C (avg. 35 °C) and between 12.7 °C and 73.5 °C (avg. 31 °C), respectively, which coincide with the same brine temperature range obtained in this work.

Regarding secondary features, all crystals registered early diagenetic processes (*i.e.*, syntaxial halite overgrowth, chevron and cornet crystals sharply truncated by dissolution, flattened crystals, tubular voids, and halite cement precipitation) typical of *syn*-depositional alteration. These features suggest an inconstant halite deposition in the basin, which was perturbated by fluid circulation, inducing dissolution and reprecipitation, as well as inflow of mud and clay, that influenced the formation of millimetric scale halite crystal. The Verzino area shows more secondary petrographic features compared to samples from Coste del Sale and Zinga areas and records the main tectonic movements in the region. Post depositional diagenetic features are testified by the presence of (a) equigranular mosaics crystals with boundaries that meet at triple junctions (~120° angles), (b) secondary FIs (mainly two-phase vapour rich), (c) necking-down (from weak to strong), (d) re-equilibration processes (stretching and leakage), and (e) different degree of fracturing (from medium to high). These features suggest ductile and plastic deformation phenomena due to temperatures and pressures increase (tectonic activity, burial and/or exhumation processes) whereby grains 'optimize' their size, shape and orientation to minimize energy. These lines of evidence suggest that these samples register early Pliocene extension or transtensional tecton-

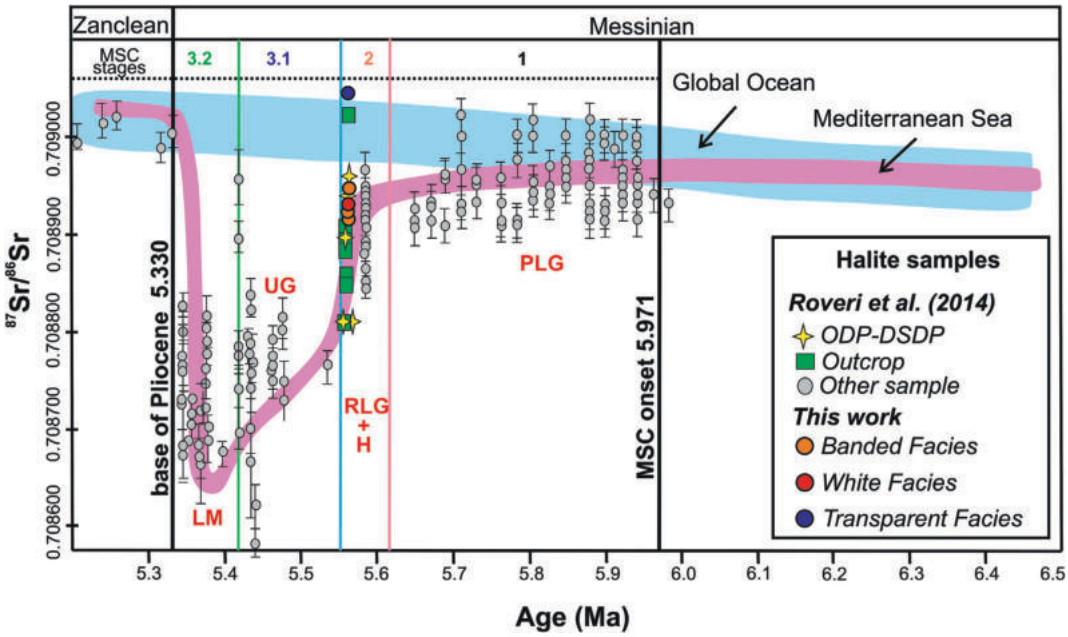

Fig. 12. Strontium isotopic ratios ($^{87}Sr/^{86}Sr$) from five halite samples, belonging to the banded, white and transparent facies compared with halite DSDP-ODP drill cores, halite outcrops and other samples reported by Roveri et al. (2014). PLG – Primary Lower Gypsum, RLG – Resedimented Lower Gypsum, H – Halite, UG – Upper Gypsum, LM – Lago Mare.

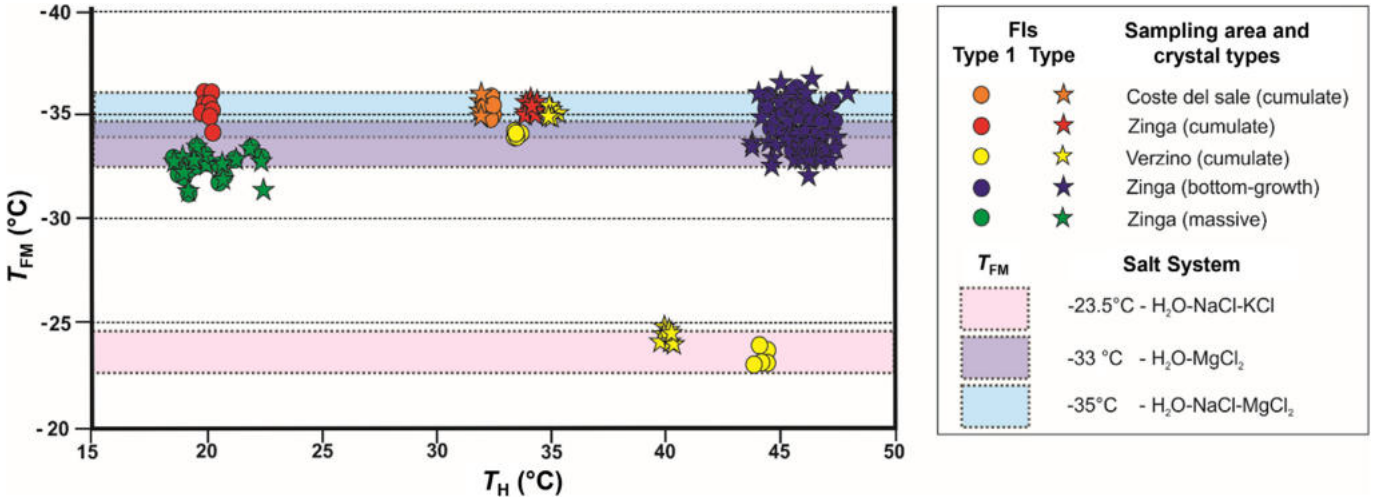

Fig. 13. Temperature of first melting (T_{FM}) *vs.* Temperature of homogenization (T_H) diagram shows the distribution of Type 1 and Type 2 FIs for each crystal type. T_{FM} is associating with water salt systems reported by Shepherd et al. (1985).

ics which allowed the Verzino salt dome to pierce the latest Messinian unit containing Lago Mare Fauna and the Cavalieri formation (early Pliocene unit).

The integrated petrographic and geochemical approach contributes to a better understanding of the depositional dynamics and environmental conditions of halite formation, allowing evaluation between shallow evaporitic and deep. Indeed, cumulate crystals may precipitate and be preserved in both shallow and deep saline settings through distinct, yet occasionally overlapping mechanisms, that are strongly modulated by hydroclimatic seasonality and water column stratification.

In shallow salt pan environments, halite can form directly at the water surface through the development of flat crystal clusters known as halite rafts. These are initially held at the surface by capillary forces, but as they grow heavier, they detach and sink to the basin floor, where they may continue to grow (Lowenstein and Hardie, 1985; Warren, 1999; Lugli et al., 2007; Tai and Aref, 2015; Lowenstein et al., 2021). A second mechanism active in these settings involves the nucleation of fine halite crystals within a supersaturated water column, particularly during winter. Under thermally and chemically stratified conditions, these crystals settle rapidly (~0.5 cm/s) and undergo minimal growth during descent, preserving their original morphology. Once deposited, calm and often anoxic bottom waters favour their accumulation and long-term preservation as finely laminated cumulate halite beds (Taj and Aref, 2015). Similar processes are observed in deep stratified basins, such as the modern Dead Sea (widely regarded as a modern analogue for the deep hypersaline basins that developed during the Messinian salinity crisis), where halite deposition and preservation are tightly linked to seasonal hydroclimatic dynamics. Thermal and hyaline gradients generate a stable pycnocline that regulates halite saturation along the water column. During summer, evaporative

concentration in the epilimnion can lead to halite undersaturation and dissolution, while the deeper, cooler hypolimnion remains supersaturated, promoting halite precipitation (Kiro et al., 2016; Sirota et al., 2017). This vertical gradient results in pronounced lateral and vertical heterogeneity in halite textures and facies. Furthermore, the generally low-energy hydrodynamic regime, with limited wind and wave activity, minimizes brine mixing and mechanical reworking, enhancing crystal preservation (Benison and Goldstein, 1999). These conditions allow the development of well-defined seasonal layering, typically alternating coarse- and fine-grained halite, reflecting changes in temperature, brine chemistry, and saturation conditions throughout the year.

Regarding banded halite facies, recognised in the Crotone Basin, the overall evidence indicates that these crystals formed under very shallow and hydrologically unstable conditions. The fine lamination of cumulate halite and the recurrent intercalation of mudstone/ siltstone layers point to cyclic flooding and dilution events, typical of ephemeral saline pans subjected to fluctuating brine levels. Dissolution and syntaxial overgrowth textures, together with tubular voids and early cementation, indicate repeated episodes of partial dissolution and reprecipitation within a chemically dynamic environment. The predominance of microcrystalline fabrics, the presence of halite rafts and chevron crystals, and the rapid recrystallization processes are consistent with surface or near-surface precipitation driven by intense evaporation. Fluid inclusion data also support a shallow depositional setting. Indeed, the measured homogenization temperatures (20 – 45 °C; avg. 34 °C) are significantly higher than those observed in deep, stratified basins but closely resemble values recorded in shallow evaporitic environments such as the Realmonte salt mine and Death Valley (Lugli and Lowenstein, 1997; Lowenstein et al., 1998). Moreover, the chemical composition of the inclusions indicates advanced evaporative concentration under restricted hydrological conditions, suggesting distinct conditions from those typical of persistent stratification or deep-water renewal.

All these observations suggest that halite precipitation occurred within a shallow, ephemeral saline pan affected by hydrological oscillations. In such an environment, alternating episodes of flooding, evaporation, and brine recycling could have produced finely laminated halite-mudstone couplets and early diagenetic overprints, supporting the interpretation that the banded facies of the Crotone Basin represent the product of shallow-water evaporitic processes.

5.1.2. Bottom-growth crystal from the white facies

The bottom-growth crystals belonging to the white facies is characterised by the direct crystallisation of halite at the sediment–water interface from saturated brines, typically under relatively low degrees of supersaturation. According to Taj and Aref (2015), this facies includes subhedral to euhedral halite crystals with well-defined growth zoning and frequent chevron morphologies, indicative of *in situ* precipitation rather than crystal settling. Crystals grow undisturbed, and their texture is formed by separate bands of a dark colour (milky bands – enriched with FIs) and light colour (clear bands – with few or absent FIs). Such zoning is the result of varying crystal growth rates (*see* Warren, 1999, 2006), with milky bands forming rapidly during periods of intense evaporation and clear bands crystallising slowly during periods of lower evaporation rates linked to pycnocline oscillations (*see* Roedder, 1984; Lowenstein and Hardie, 1985). This growth pulse creates primary textures referred to as "chevron fabric". Each pulse is characterised either by thin layers of less saline salts or by inclusions of brine that were poikilitically enclosed during crystal precipitation. This style of microlaminated crystal layering reflects changes in crystal precipitation rates induced by short-term changes (daily to monthly) in salinity on the subaqueous floor of the brine pan (Hanford, 1991; Warren, 1999).

Bottom-growth crystals are commonly associated with desiccation and partial dissolution of crystals due to freshwater inflow (*e.g.*, Casas and Lowenstein, 1989); in fact, in shallow brines, a freshwater flood entering the brine may cause mixing of the water column, which reduces the degree of saturation of halite and in turn causes dissolution (Lowenstein and Hardie, 1985).

Zi-07 and Zi-09 samples preserve well chevron fabric. Indeed, they show only scarce syn- or post-depositional features, including bands occasionally interrupted by sharp and curved dissolution surfaces, consistent with the salt dome evolution of this deposit, suggesting a minimal burial and/or exhumation (diapiric upwelling).

Regarding primary features, in the Zi-09 sample, 56 pulses in 2.5 cm of crystal are counted; using data from Schreiber and Hsü (1980), who estimate a rate of approximately 10 m per 1000 years (~1 cm per year), the pulses are formed in ~ 28 days; however, considering the modern halite precipitation in the Dead Sea (Sirota et al., 2017 and references therein), the growth rate is ~ 0.1 m/yr, which results in ~ 3 months for Zi-09 sample. The different rates of halite precipitation depend on continental water input and/or physicochemical and climatic factors (*e.g.*, salinity, temperature) that are reflected in a different water balance.

The fast growth of milky bands could be derived from (i) high brine temperature and/or (ii) periodic variation in organic material content during crystal growth. Zi-07 and Zi-09 samples demonstrate the coexistence of these two variables. Microthermometric analyses show high brine temperatures between 44 °C and 50 °C, suggesting a hypersaline environment and scarce continental inflow. While periodic variation in organic material content during crystal growth is evidenced by the bright UV-epifluorescence recognised in milky bands, by amorphous carbonaceous material detected under SEM observations and by traces of organic-rich remains trapped within Type 3 FIs. The presence of organic material is confirmed by Raman analysis, which revealed, in addition to the typical halite peak (358 cm^{-1}), bumps in correspondence of G- and D-bands (1345 cm^{-1} and 1600 cm^{-1}) characteristics of organic remains (Guido et al., 2018, 2022). The presence of such organic compounds may not only reflect *syn*-depositional biological activity or the incorporation of decaying biomass but may also have actively contributed to the nucleation and crystallisation of halite. As demonstrated by Jagniecki and Beninson (2010), halite can precipitate directly from supersaturated brines in the presence of acidic organic compounds, which act as heterogeneous nucleation agents. These compounds modify the local physicochemical conditions of the brine, effectively reducing the activation energy required for halite crystal formation. The resulting halite, termed acid-precipitated halite, often displays characteristic micro textures, such as fine-grained, poorly aligned crystals, potentially analogous to some of the microcrystalline textures observed in the studied samples.

Additional evidence for organic-mediated halite formation comes from Schubert et al. (2010a), who observed that halophilic microbial communities inhabiting brine environments can promote halite precipitation through both passive and active processes. Microbial EPS (extracellular polymeric substances), in particular, provide nucleation surfaces that trap ions and create localized microenvironments conducive to crystal growth. Moreover, the decay of microbial cells and organic residues alters the ionic composition and pH of the surrounding microhabitats, further modulating mineral saturation states. In this context, the organic matter detected in samples from the Crotone Basin, supported by SEM, Raman spectroscopy, and UV-epifluorescence, may have acted as both a record of past biological activity and a

catalyst for halite nucleation, influencing crystal size, morphology, and fluid inclusion textures.

Therefore, the observed association between organic matter and halite may not be indicative of a biogeochemically influenced precipitation mechanism, but it may be related to processes influencing both the microstructure and the diagenetic evolution of the halite. As previously observed in the cumulate crystals, the eutectic point measured for bottom-growth crystals suggests an original H_2O-NaCl-$MgCl_2$ brine composition (Fig. 13) in agreement with an advanced evaporative state, a condition of extreme supersaturation, and a salinity range 70 – 90 times higher than the original seawater (> 340 ‰ – 360 ‰).

As shown for the T_H determined in cumulate crystals, T_H obtained in white facies (T_H > 45 °C) agree with the data of Galamay et al. (2023), which indicated brine temperature between 12.7 °C and 73.5 °C (avg. 31 °C). These elevated temperatures may explain the abundant presence of bassanite and anhydrite in Type 3 FIs, as observed under synchrotron and confirmed by SEM-EDS analyses. Indeed, the transformation of gypsum into bassanite or anhydrite typically occurs at relatively high ambient temperatures and/or high brine salinities (*e.g.*, > 45 °C; Mahmoud et al., 2015), and these phases may appear either as solid inclusions or as daughter minerals. In contrast, the lower average T_H (~18 °C) reported by Speranza et al. (2013) from samples of the same salt deposit most likely reflects fluid trapped in halite layers that precipitated under different brine conditions. This apparent discrepancy may be attributed to stratigraphic and textural variability within the salt dome, as the samples analysed in our study come from different levels or facies that may have recorded distinct environmental or diagenetic histories. Therefore, the observed range in T_H values should not be interpreted as a contradiction, but rather as a reflection of the complex thermal and geochemical evolution of the halite body.

5.1.3. Massive crystals from the transparent facies

Massive halite crystals, characterised by translucent and opaque halite and herein classified within the newly defined transparent facies, had not been previously documented in the Crotone Basin or other Mediterranean Messinian settings. While macro- and *meso*-scale observations initially suggested complete recrystallisation, detailed micro- and nano-scale analyses combined with SEM-EDS investigations revealed critical features that challenge this interpretation. Specifically, (i) the absence of pagoda halite crystals on translucent crystal surfaces, (ii) aligned trails of primary fluid inclusions (FIs), and (iii) Type 3 FIs containing remnants of organic matter collectively indicate that these crystals are not fully recrystallised.

In contrast, the opaque portions of the crystals (unobservable under optical microscopy) revealed, through SEM analysis, distinctive structural features such as pagoda morphologies and surface ridges. Pagoda crystals form through preferential NaCl precipitation on crystal edges rather than faces, representing progressive increases in precipitation rate under specific physicochemical conditions (Southgate, 1982). Their occurrence, alongside curved regrowth morphologies that truncate original hopper planes, implies episodes of partial dissolution and regrowth, rather than pervasive diagenetic overprinting.

Furthermore, the crystals display intergranular voids and secondary FIs exhibiting necking-down and stretching textures, indicative of tectonic stress effects, potentially associated with salt dome evolution. SEM-EDS elemental analyses confirm the crystals' composition as predominantly made by sodium (~29.5 wt.%), chloride (~63.4 wt.%), and potassium (~7.1 wt.%), and this is consistent across both translucent and opaque domains.

The low temperature of the brine (between +18 °C and +22 °C), combined with the absence of chevron fabric, suggests a preferential halite growth along the depressed outer rim of the evaporative basin, where the brine was at deepest levels and evaporation was most intense (*see* Arthurton, 1973; Southgate, 1982). This localized deepening likely created conditions favourable to the development of massive crystals, with fewer interruptions from wave action or sediment input. According to Southgate (1982), such marginal zones of saline basin often record episodic inflows or evaporative concentration, which contribute to the formation of larger, more transparent halite crystals with smooth faces and minimal inclusions.

Considering the stratigraphic position of the massive crystals lying above the bottom-growth crystals, and their limited areal extent, it is more plausible that these crystals reflect a transitory phase of increased water depth, possibly triggered by localized subsidence, renewed inflow of less saline water, or temporary flooding events. Such environmental shifts could have temporarily stabilized the brine composition and reduced sediment influx, allowing crystals to grow undisturbed and favouring the development of clearer and massive halite.

5.2. $^{87}Sr/^{86}Sr$ ratios – mixing processes

The Sr isotope ratio of water, in a partially closed basin connected to the global ocean, is controlled by simple mixing between ocean water and other water sources feeding the basin (*e.g.*, river run-off and rainwater) (Ingram and Sloan, 1992; Reinhardt et al., 1998). The Mediterranean evaporites incorporated the Sr of the water from which crystals precipitated without Sr-isotope fractionation, and therefore, their $^{87}Sr/^{86}Sr$ can provide important information on the origin of brine in the basin (continental or marine). As reported by several authors (*e.g.*, Ingram and Sloan, 1992; Reinhardt et al., 1998; Flecker and Ellam, 2006, Topper et al., 2011; Andreetto et al., 2021; Flecker et al., 2022) the degree of mixing between oceanic and externally sourced water (*e.g.*, river water) can be estimated by calculating the difference in the $^{87}Sr/^{86}Sr$. During the MSC, in most Mediterranean marginal basins (*e.g.*, Schildgen et al., 2014), the predominance of Mesozoic carbonates, characterised by a $^{87}Sr/^{86}Sr$ ratio between ~0.7071 and ~0.7076 (McArthur et al., 2012), resulted in a relative decreasing of the $^{87}Sr/^{86}Sr$ ratio as a consequence of the local run-off. The final isotopic signature could be similar to a mixture of the three potential sources of the Mediterranean Basin: (i) Atlantic (~0.7090 during the late Messinian; McArthur et al., 2012); (ii) main Mediterranean rivers (*e.g.*, the Nile with 0.7060 and Rhône with 0.7087; Brass, 1976; Albarede and Michard, 1987), and (iii) Eastern Paratethys (0.7084 – 0.7085; Grothe et al., 2020), making local and Oceanic inputs challenging to distinguish (Andreetto et al., 2021).

By contrast, the Crotone Basin in NE Calabria is characterised by fluvial catchments dominated by Palaeozoic Crystalline Units (*e.g.*, the Sila Unit; Van Dijk et al., 2000; Borrelli et al., 2022). Rivers draining these rocks have substantially higher $^{87}Sr/^{86}Sr$ ratios (> 0.7100 on average, *e.g.*, Toscani et al., 1990; Conticelli et al., 2009). This contrast makes it possible to distinguish the local fluvial supply to this Calabrian marginal basin from the lower Sr isotope ratios of the Mediterranean's water sources.

Regarding the cumulate crystals collected in all investigated areas, they highlighted $^{87}Sr/^{86}Sr$ values of 0.708950, 0.708918, and 0.708934 (CS-01, Zi-01, and Ve-01 samples, respectively). These results are in agreement with Roveri et al. (2014), who place the halite samples from the East-Mediterranean in a $^{87}Sr/^{86}Sr$ range from 0.708800 to 0.709000, corresponding to the second stage of the MSC during the halite deposition at TG14 and TG12 isotope stages (ca. 5.61 – 5.55 Ma; Clauzon et al., 1996; Vidal et al., 2002; Roveri et al., 2008a,b).

On the other hand, Bottom-growth (white) and Massive (transparent) crystals, representative of the Zinga sampling area, have

shown $^{87}Sr/^{86}Sr$ values of 0.708934 and 0.709054, respectively. These values are also in agreement with Roveri et al. (2014). If the entire Zinga succession (Cumulate, Bottom-growth, and Massive) is considered, a gradual increase in the isotope ratio is observed up to values even higher than the expected average for oceanic water during the late Messinian (~0.7090; McArthur et al., 2012). Based on the above, this positive shift could represent an increase in local continental input, representative of a granitic-crystalline basement. This would testify to the presence of a more diluted water mass in transparent facies concerning the cumulate and bottom-growth crystals, further corroborated by the lower temperatures recognised for the "transparent" brine (from +18 °C to +22 °C).

5.3. Implications of synchrotron-based 3D imaging for halite growth and basin dynamics

The integration of synchrotron-based X-ray microtomography provided a unique opportunity to visualise the internal structure of Messinian halite crystals in three dimensions, offering new insights into their growth dynamics and the environmental conditions of deposition. One of the most significant observations emerging from this technique is the lack of pervasive recrystallisation across white and transparent facies. The preservation of primary microstructures is a key prerequisite for a reliable interpretation of halite growth history.

The scarce presence of recrystallisation features, such as grain boundary migration, fractures or fluid inclusions affected by re-equilibration phenomena, confirm that the halite facies retained their original depositional fabrics. The textural integrity of these fabrics is critical because it enables the use of crystal morphology and inclusion distribution as proxies for interpreting the hydrological and geochemical conditions during crystal growth.

Synchrotron microtomography allowed the non-destructive, three-dimensional visualisation of halite crystals at high resolution (down to a few microns), revealing internal features not accessible by traditional 2D petrography. For instance, the distribution of fluid inclusions in the white and transparent facies occurs in organised, layered patterns or as clusters aligned along growth zones, indicating cyclic or pulsatory brine inflow and rapid precipitation events.

The internal architecture of the halite crystals, as revealed by 3D imaging, also correlated strongly with microthermometric and isotopic data, reinforcing the interpretation of distinct facies-specific thermal regimes and brine compositions. Indeed, the relatively low temperature and increased Sr isotopic ratio observed in the transparent facies align with the presence of large, fluid-rich cavities and massive crystal structures, suggesting a more diluted brine and slower crystal growth in a possibly more open hydrological system.

5.4. Organic materials

The presence and distribution of organic materials within halite crystals and their associated fluid inclusions provide critical insights into the environmental conditions and potential biotic interactions during crystal formation. Raman analyses revealed a variety of trapped organic substances, including elongated transparent filaments, amorphous compounds, and pigmented cellular matter. The filaments, displaying a strong blue fluorescence under UV and a convolute morphology, are tentatively attributed to cyanobacteria of the *Oscillatoriales* genus, organisms typically thriving in shallow, well-mixed aquatic environments (Reynolds et al., 2002). In addition, the red/orange organic inclusions, which exhibit intense red fluorescence, likely correspond to *Dunaliella* spp., halophilic microalgae capable of surviving in hypersaline conditions and known for producing high concentrations of β-carotene and glycerol (Schubert et al., 2009, 2010a,b; Lowenstein et al., 2011; Sankaranarayanan et al., 2011). This interpretation is further supported by Raman detection of carotene-related spectral peaks.

Amorphous organic materials, ranging in colour from yellow to brown and black, were also observed, particularly within Type 3 fluid inclusions and among the crystals. These materials yielded Raman signatures consistent with low-maturity organic matter, including G- and D-bands (1345 cm^{-1} and 1600 cm^{-1}), as well as methyl and methylene group vibrations near 2885 – 2930 cm^{-1} (Guido et al., 2018, 2019b, 2022; Bukowski et al., 2020; Adar, 2021). Their occurrence in both crystal lattice and inclusions suggests episodic enrichment of the brine in organic material during halite precipitation. While the data do not conclusively demonstrate whether this organic matter was *in situ* microbially derived or passively incorporated from external sources, their localization and spectral features are compatible with the intermittent input of carbonaceous compounds during crystal growth.

These observations align with findings from previous studies showing microorganisms (*i.e.* halophilic archaea) not only survive within fluid inclusions but may actively influence halite crystallisation processes. Specifically, their presence has been shown to promote the formation of larger halite crystals, increase the size and abundance of fluid inclusions, and induce dendritic morphologies (López-Cortés et al., 1994; Grant et al., 1998; Le Métayer-Levrel et al., 1999; McGenity et al., 2000). Furthermore, organic compounds such as microbial necromass and hydrocarbons, like those occasionally trapped within inclusions, may serve as energy and carbon sources for long-term microbial survival within ancient halite deposits (Pironon et al., 1995; McGenity et al., 2000).

Overall, the results suggest a possible dual role of organic matter in halite formation: (i) as modulator of crystal morphology, potentially influencing nucleation and growth dynamics, and (ii) as reservoir within primary fluid inclusions, which may have sustained halophilic microbial communities over extended time scales.

Although the investigation of organic compounds was not the primary focus of this study, our findings highlight the need for specific molecular and isotopic analyses of the preserved organic matter. Such studies are essential to verify these hypotheses and to identify the original microbiome and/or specific biomolecules that may have played a role in the biomineralisation processes.

5.5. Integrated paleoenvironmental model and implications for basin evolution

The halite deposits of the Crotone Basin are interpreted as the result of precipitation within a salt pan or saline mudflat system, in agreement with the model proposed by Lugli et al. (2010). This environment, likely shallow and hydrologically unstable, was characterised by repeated cycles of flooding, dilution, and strong seasonal variability. These dynamics produced distinct salinity regimes, reflected in the deposition of the three halite facies (banded, white, and transparent) each capturing a specific stage in the evolution of the evaporative system.

The banded facies, widespread across Coste del Sale, Zinga, and Verzino, is composed of alternating cumulate halite beds and mud-rich layers. Primary textures such as subhedral-euhedral crystals and chevron patterns, together with the presence of primary fluid inclusions and poor-intercrystalline cementation, point to only partial diagenetic overprint, in contrast to the interpretation of a fully recrystallized facies in Verzino by Lugli et al. (2007). These features indicate shallow, marginal depositional conditions with intermittent detrital and possibly microbial input, consistent with modern analogues described by Hovorka et al. (2007).

The Coste del Sale succession is of particular significance, as it preserves *in situ* halite directly overlying the Calcare di Base (limestone formation). Unlike the Zinga and Verzino deposits, where halite is exposed due to diapirism, this stratigraphic context offers a unique opportunity to reconstruct the original precipitation setting. The preservation of architectural features, $^{87}Sr/^{86}Sr$ isotopic ratios, and fluid inclusion assemblages supports a primary depositional origin during the early phase of the Messinian Salinity Crisis, offering key insights into paleogeographic and hydrological conditions across the basin.

The white facies, dominated by chevron-textured bottom-growth crystals with alternating milky and clear bands, records halite crystallisation at the sediment-brine interface under variable brine chemistry and supersaturation dynamics, potentially driven by pycnocline oscillations (Lowenstein and Hardie, 1985; Warren, 1999). The presence of primary fluid inclusions, elevated homogenization temperatures, and solid inclusions such as bassanite and anhydrite, indicates deposition from hypersaline and thermally elevated brines. Furthermore, the detection of organic matter suggests putative biotic mediation in nucleation processes, as previously described for microbial mats in brine systems (Jagniecki and Beninson, 2010; Schubert et al., 2010a,b).

The transparent facies, unique to the Crotone Basin, is composed of massive halite crystals with translucent and opaque domains. While initially interpreted as fully recrystallized, detailed petrographic and SEM observations revealed the presence of growth zoning, aligned primary inclusions, and organic-rich sectors, arguing against pervasive diagenesis. The presence of pagoda halite morphologies (*sensu*; Southgate, 1982) in the opaque zones indicates episodic growth under fluctuating physicochemical conditions. These features, together with partial dissolution-regrowth textures and relatively low homogenization temperatures (18 – 22 °C), support a model of precipitation in a more stable, stratified subaqueous environment, possibly related to localized deepening or brine recharge during the late stages of halite accumulation.

Together, these findings delineate a coherent facies evolution model from shallow, intermittently exposed and biologically active marginal zones (banded, white) to a more chemically buffered and spatially restricted central-basin environment (transparent). The integration of sedimentological, petrographic, geochemical, and spectroscopic data underlines the critical role of organic matter input, brine evolution, and early diagenetic processes in shaping the internal architecture and textural variability of Messinian halite.

6. Conclusions

This study integrated petrographic, geochemical, and spectroscopic data to reconstruct the depositional history of Messinian halite in the Crotone Basin. The identification and characterisation of three halite facies (banded, white, and transparent) revealed distinct physicochemical and paleoenvironmental conditions during halite precipitation.

The banded facies formed in marginal, shallow settings under fluctuating hydrological regimes, preserving primary textures despite minor diagenetic overprint. The white facies reflects dynamic brine evolution, with variable salinity, organic input, and evidence of microbial influence on crystal growth. The transparent facies indicated halite formation from stable, stratified brines, with limited organic content and minimal post-depositional modification.

Overall, these facies represent a continuum of depositional environments shaped by salinity dynamics, organic matter availability, and basin-scale hydrological changes. Their combined analysis offers new insights into the complexity of evaporite formation during the Messinian Salinity Crisis and highlights the value of halite as a proxy for reconstructing past environmental conditions in evaporite settings.

Moreover, the presence of organic materials, including microbial filaments and low-maturity compounds, within halite crystals and fluid inclusions highlights the potential role of biological processes in mineral nucleation and brine evolution. These findings emphasize the complexity of evaporite formation in extreme environments and open new avenues for investigating the interactions between biological, chemical, and physical processes in both modern and ancient hypersaline systems.

CRediT authorship contribution statement

Mara Cipriani: Writing – review & editing, Writing – original draft, Visualization, Validation, Supervision, Software, Resources, Project administration, Methodology, Investigation, Formal analysis, Data curation, Conceptualization. **Alessandra Costanzo:** Writing – review & editing, Visualization, Validation, Supervision, Methodology, Conceptualization. **Martin Feely:** Writing – review & editing, Visualization, Validation, Supervision, Methodology. **Adriano Guido:** Writing – review & editing, Visualization, Validation, Supervision, Methodology, Investigation, Conceptualization. **Massimo D'Antonio:** Writing – review & editing, Validation, Methodology, Investigation, Conceptualization. **Giovanni Vespasiano:** Writing – review & editing, Validation, Investigation, Conceptualization. **Sandro Donato:** Writing – review & editing, Visualization, Software, Methodology, Funding acquisition, Formal analysis. **Giuseppe Cianflone:** Writing – review & editing, Validation, Conceptualization. **Giuseppe Maruca:** Writing – review & editing, Visualization, Validation, Conceptualization. **Carmine Apollaro:** Writing – review & editing, Validation, Conceptualization. **Francesca Alessandro:** Writing – review & editing, Visualization, Methodology, Formal analysis. **Francesco Perri:** Writing – review & editing, Validation, Conceptualization. **Rocco Dominici:** Writing – review & editing, Visualization, Validation, Supervision, Methodology, Investigation, Funding acquisition, Conceptualization.

Declaration of competing interest

The authors declare that they have no known competing financial interests or personal relationships that could have appeared to influence the work reported in this paper.

Acknowledgments

We sincerely thank the Editor and the two anonymous Reviewers for their constructive comments and valuable suggestions, which have greatly contributed to improving the quality and clarity of the manuscript. We would also like to express our gratitude to Dr Mario Cimieri and *Halite Associazione* for their commitment in the safeguarding of the entire area and support of this research. This research is part of Mara Cipriani's unpublished PhD thesis, titled: "Facies analysis and fluid inclusion studies of the Messinian evaporites, Calabria, Southern Italy" and financially supported by the SIACE doctoral school (University of Calabria) and with the agreement with "C/Terzi General Mining Research Italy", with funding secured by Rocco Dominici.

Sandro Donato is supported by the project Tech4You- Technologies for climate change adaptation and quality of life improvement (C.I. ECS 00000009, CUP H23C22000370006).

References

Adamuszek, M., Tămaş, D.M., Barabasch, J., Urai, J.L., 2021. Rheological stratification in impure rock salt during long-term creep: morphology, microstructure, and numerical models of multilayer folds in the Ocnele Mari salt mine, Romania. Solid Earth 12 (9), 2041–2265. https://doi.org/10.5194/se-12-2041-2021.

Adar, F., 2021. A simple introduction to Raman spectral identification of organic materials. Spectroscopy 36 (11), 8–15. https://doi.org/10.56530/spectroscopy.ol8176c6.

Agiadi, K., Hohmann, N., Gliozzi, E., Thivaiou, D., Bosellini, F.R., Taviani, M., Bianucci, G., Collareta, A., Londeix, L., Faranda, C., Bulian, F., Koskeridou, E., Lozar, F., Mancini, A.M., Dominici, S., Moissette, P., Campos, I.B., Borghi, E., Iliopoulos, G., Antonarakou, A., Kontakiotis, G., Besiou, E., Zarkogiannis, S.D., Harzhauser, M., Sierro, F.J., Coll, M., Vasiliev, I., Camerlenghi, A., García-Castellanos, D., 2024. The marine biodiversity impact of the Late Miocene Mediterranean salinity crisis. Science 385, 986–991. https://doi.org/10.1126/science.adp3703.

Albarede, F., Michard, A., 1987. Evidence for slowly changing 87Sr/86Sr in runoff from fresh-water limestones of southern France. Chem. Geol. 64 (1–2), 55–65. https://doi.org/10.1016/0009-2541(87)90151-3.

Aloisi, G., Moneron, J., Guibourdenche, L., Camerlenghi, A., Gavrieli, I., Bardoux, G., Agrinier, P., Ebner, R., Gvitzman, Z., 2024. Chlorine isotopes constrain a major drawdown of the Mediterranean Sea during the Messinian salinity crisis. Nat. Commun. 15, 9671. https://doi.org/10.1038/s41467-024-53781-6.

Andreetto, F., Aloisi, G., Raad, F., Heida, H., Flecker, R., Agiadi, K., Lofi, J., Blondel, S., Bulian, F., Camerlenghi, A., Caruso, A., Ebner, R., Garcia-Castellanos, D., Gaullier, V., Guibourdenche, I., Gvirtzman, Z., Hoyle, T.M., Meijer, P.T., Moneron, J., Sierro, F.J., Travan, G., Tzevahirtzian, A., Vasiliev, I., Krijgsman, W., 2021. Freshening of the Mediterranean Salt Giant: controversies and certainties around the terminal (Upper Gypsum and Lago-Mare) phases of the Messinian salinity crisis. Earth Sci. Rev. 216, 103577. https://doi.org/10.1016/j.earscirev.2021.103577.

Arthurton, R.S., 1973. Experimentally produced halite compared with Triassic layered halite-rock from Cheshire, England. Sedimentology 20 (1), 145–160. https://doi.org/10.1111/j.1365-3091.1973.tb01611.x.

Bąbel, M., Schreiber, B.C., 2014. Geochemistry of evaporites and evolution of seawater. In: Holland, H., Turekian, K. (Eds.), Treatise on Geochemistry (2nd Edition). Elsevier, pp. 483–560.

Bakker, R.J., Jansen, B.H., 1990. Preferential water leakage from fluid inclusions by means of mobile dislocations. Nature 345, 6270, 58–60. https://doi.org/10.1038/345058a0.

Barone, M., Dominici, R., Muto, F., Critelli, S., 2008. Detrital modes in a late Miocene wedge-top basin, Northeastern Calabria, Italy: Compositional record of wedge-top partitioning. J. Sediment. Res. 78, 693–711. https://doi.org/10.2110/jsr.2008.071.

Bein, A.S.D., Hovorka, R.S.F., Roedder, E., 1991. Fluid inclusions in bedded Permian halite, Palo Duro, Texas: evidence for modification of seawater in evaporite brine-pools and subsequent early diagenesis. J. Sediment. Petrol. 61, 1–14. https://doi.org/10.1306/D4267672-2B26-11D7-8648000102C1865D.

Benison, K.C., Goldstein, R.H., 1999. Permian paleoclimate data from fluid inclusions in halite. Chem. Geol. 154 (1), 113–132. https://doi.org/10.1016/S0009-2541(98)00127-2.

Birgel, D., Guido, A., Liu, X., Hinrichs, K.U., Gier, S., Peckmann, J., 2014. Hypersaline conditions during deposition of the Calcare di Base revealed from archaeal di- and tetraether inventories. Org. Geochem. 77, 11–21. https://doi.org/10.1016/j.orggeochem.2014.09.002.

Bodnar, R.J., Bethke, P.M., 1984. Systematics of stretching of fluid inclusions. Part I. Fluorite and sphalerite at 1 atmosphere confining pressure. Econ. Geol. 79, 141–161. https://doi.org/10.2113/gsecongeo.79.1.141.

Borrelli, M., Perri, E., Avagliano, D., Coraggio, F., Critelli, S., 2022. Paleogeographic and sedimentary evolution of North Calabrian basins during the Messinian Salinity Crisis (South Italy). Mar. Pet. Geol. 141. https://doi.org/10.1016/j.marpetgeo.2022.105726.

Brass, G.W., 1976. The variation of marine $^{87}Sr/^{86}Sr$ ratio during Phanerozoic time: Interpretation using a flux model Geochim. Cosmochim. Acta 40, 721–730. https://doi.org/10.1016/0016-7037(76)90025-9.

Brennan, S.T., Lowenstein, T.K., Horita, J., 2004. Seawater chemistry and the advent of biocalcification. Geology 32 (6), 473–476. https://doi.org/10.1130/G20251.1.

Brombal, L., Donato, S., Dreossi, D., Arfelli, F., Bonazza, D., Contillo, A., Delogu, P., Di Trapani, V., Golosio, B., Mettivier, G., Oliva, P., Rigon, L., Taibi, A., Longo, R., 2018. Phase-contrast breast CT: the effect of propagation distance. Phys. Med. Biol. 63, 24NT03.

Brun, F., Pacilè, S., Accardo, A., Kourousias, G., Dreossi, D., Mancini, L., Tromba, G., Pugliese, R., 2015. Enhanced and flexible software tools for X-ray computed tomography at the Italian synchrotron radiation facility Elettra. Fundamenta Informaticae 141, 233–243. https://doi.org/10.3233/FI-2015-1273.

Bukowski, K., Galamay, A., Krzywiec, P., Maksym, A., 2020. Geochemical data and fluid Inclusion study of the Middle Miocene halite from deep borehole Huwniki-1, situated in the inner zone of the Carpathian foredeep in Poland. Minerals 10, 1113. https://doi.org/10.3390/min10121113.

Casas, E., Lowenstein, T.K., 1989. Diagenesis of saline pan halite: comparison of petrographic features of modern, Quaternary, and permian halites. J. Sediment. Petrol. 59, 724–739.

CIESM, 2008. The Messinian salinity crisis from mega-deposits to microbiology. A consensus report. In: Briand, F., Monaco (Eds.), 33ème CIESM Workshop Monographs, 33, 91–96.

Cipriani, M., Donato, S., Alessandro, F., Campilongo, G., Cianflone, G., Costanzo, A., Guido, A., Lanzafame, G., Magarò, P., Maletta, C., Maruca, G., Dominici, R., 2024a. Can crystal imperfections alter the petrophysical properties of halite minerals? Mar. Pet. Geol. 155, 106407. https://doi.org/10.1016/j.marpetgeo.2023.106407.

Cipriani, M., Apollaro, C., Basso, D., Bazzicalupo, P., Bertolino, M., Bracchi, V.A., Bruno, F., Costa, G., Dominici, R., Gallo, A., Muzzupappa, M., Rosso, A., Sanfilippo, R., Sciuto, F., Vespasiano, G., Guido, A., 2024b. Origin and role of non-skeletal carbonate in coralligenous build-ups: new geobiological perspectives in biomineralization processes. Biogeosciences 21 (1), 49–72. https://doi.org/10.5194/bg-21-49-2024.

Cipriani, M., Dominici, R., Costanzo, A., Vespasiano, G., Apollaro, C., Miriello, D., Cianflone, G., Perri, F., D'Antonio, M., Maruca, G., Guido, A., 2023a. Messinian resedimented gypsum (branching-like facies) from the Catanzaro Basin (Calabria, Southern Italy): petrographic and geochemical evidence for paleoenvironmental reconstruction. Rend. Online Soc. Geol. It. 59, 35–39. https://doi.org/10.3301/ROL.2023.06.

Cipriani, M., Basso, D., Bazzicalupo, P., Bertolino, M., Bracchi, V.A., Bruno, F., Costa, G., Dominici, R., Gallo, A., Muzzupappa, M., Rosso, A., Perri, F., Sanfilippo, R., Sciuto, F., Guido, A., 2023b. The role of non-skeletal carbonate component in Mediterranean Coralligenous: new insight from the CRESCIBLUREEF project. Rend. Online Soc. Geol. It. 59, 75–79. https://doi.org/10.3301/ROL.2023.12.

Cipriani, M., Dominici, R., Costanzo, A., D'Antonio, M., Guido, A., 2021. A Messinian gypsum deposit in the Ionian Forearc Basin (Benestare, Calabria, southern Italy): Origin and paleoenvironmental indications. Minerals 11, 1305. https://doi.org/10.3390/min11121305.

Clauzon, G., Suc, J.-P., Gautier, F., Berger, A., Loutre, M.F., 1996. Alternate interpretation of the Messinian salinity crisis, controversy resolved? Geology 24, 363–366.

Conticelli, S., Marchionni, S., Rosa, D., Giordano, G., Boari, E., Avanzinelli, R., 2009. Shoshonite and sub-alkaline magmas from an ultrapotassic volcano: Sr-Nd-Pb isotope data on the Roccamonfina volcanic rocks, Roman Magmatic province, southern Italy. Contrib. Miner. Petrol. 157, 41–63.

Costanzo, A., Cipriani, M., Feely, M., Cianflone, G., Dominici, R., 2019. Messinian twinned selenite from the Catanzaro Trough, Calabria, Southern Italy: field, petrographic and fluid inclusion perspectives. Carbonates Evaporites 34, 743–756. https://doi.org/10.1007/s13146-019-00516-0.

Davis, D.W., Lowenstein, T.K., Spencer, R.J., 1990. Melting behaviour of fluid inclusions in laboratory-grown halite crystals in the systems NaCl-H_2O, NaCl-KCl-H_2O, NaCl-$MgCl_2$-H_2O and NaCl-$CaCl_2$-H_2O. Geochim. Cosmochim. Acta 54, 591–601. https://doi.org/10.1016/0016-7037(90)90355-O.

Debois, G., Urai, J., De Bresser, J.H.P., 2012. Fluid distribution in grain boundaries of natural fine-grained rock salt deformed at low differential stress (Qom Kuh salt fountain, central Iran): Implications for rheology and transport properties. J. Struct. Geol. 43, 128–143. https://doi.org/10.1016/j.jsg.2012.07.002.

Deines, P., Goldstein, S.L., Oelkers, E.H., Rudnick, R.L., Walter, L.M., 2003. Standards for publication of isotope ratio and chemical data in Chemical Geology. Chem. Geol. 202, 1–4. https://doi.org/10.1016/j.chemgeo.2003.08.003.

Dominici, R., Costanzo, A., Guido, A., Maruca, G., Perri, F., Molinaro, D., Cipriani, M., 2025. Short-term climate oscillations during the Messinian Salinity Crisis: new insights from Gypsum 1 lithofacies of the Crati Basin (Lattarico, Calabria, Southern Italy). Minerals 15 (5), 542. https://doi.org/10.3390/min15050542.

Donato, P., Donato, S., Barba, L., Crisci, G.M., Crocco, M.C., Davoli, M., Filosa, R., Formoso, V., Niceforo, G., Pastrana, A., Solano, A., De Rosa, R., 2022. Influence of chemical composition and microvesiculation on the chromatic features of the obsidian of Sierra de las Navajas (Hidalgo, Mexico). Minerals 12 (2), 177. https://doi.org/10.3390/min12020177.

Dullin, C., di Lillo, F., Svetlove, A., Albers, J., Wagner, W., Markus, A., Sodini, N., Dreossi, D., Alves, F. and Tromba, G., 2021. Multiscale biomedical imaging at the SYRMEP beamline of Elettra - Closing the gap between preclinical research and patient applications. Phys. Open 6, 100050. https://doi.org/10.1016/j.physo.2020.100050.

Fauquette, S., Suc, J.P., Bertini, A., Popescu, S.M., Warny, S., Taoufiq, N.B., Villa, M.J.P., Chikhi, H., Feddi, N., Subally, D., Clauzon, G., Ferrier, J., 2006. How much did climate force the Messinian salinity crisis? Quantified climatic conditions from pollen records in the Mediterranean region. Palaeogeogr. Palaeoclimatol. Palaeoecol. 238, 281–301. https://doi.org/10.1016/j.palaeo.2006.03.029.

Flecker, R., de Villiers, S., Ellam, R.M., 2002. Modelling the effect of evaporation on the salinity – $^{87}Sr/^{86}Sr$ relationship in modern and ancient marginal-marine systems: the Mediterranean Messinian. Earth Planet. Sci. Lett. 203, 221–233. https://doi.org/10.1016/S0012-821X(02)00848-8.

Flecker, R., Ellam, R.M., 2006. Identifying Late Miocene episodes of connection and isolation in the Mediterranean-Paratethyan realm using Sr isotopes. Sed. Geol. 188–189, 189–203. https://doi.org/10.1016/j.sedgeo.2006.03.005.

Flecker, R., Krijgsman, W., Capella, W., De Castro Martíns, C., Dmitrieva, E., Mayser, J. P., Marzocchi, A., Modestu, S., Ochoa, D., Simon, D., Tulbure, M., Van den Ber, B., Van der Schee, M., De Lange, G., Ellam, R., Govers, R., Gutjahr, M., Hilgen, F., Kouwenhoven, T., Lofi, J., Meijer, P., Sierro, F.J., Bachiri, N., Barhoun, N., Alami, A. C., Chacon, B., Flores, J.A., Gregory, J., Howard, J., Lunt, D., Ochoa, M., Pancost, R., Vincent, S., Yousfi, M.Z., 2015. Evolution of the Late Miocene Mediterranean–Atlantic gateways and their impact on regional and global environmental change. Earth Sci. Rev. 150, 365–392. https://doi.org/10.1016/j.earscirev.2015.08.007.

Galamay, A., Karakaya, M.Ç., Bukowski, K., Karakaya, N., Yaremchuk, Y., 2023. Geochemistry of brine and paleoclimate reconstruction during sedimentation of Messinian salt in the Tuz Gölü basin (Türkiye): Insights from the study of fluid inclusions. Minerals 13 (2), 171. https://doi.org/10.3390/min13020171.

Garcia-Castellanos, D., Villasenõr, A., 2011. Messinian salinity crisis regulated by competing tectonics and erosion at the Gibraltar arc. Nature 480, 359–363. https://doi.org/10.1038/nature10651.
García-Veigas, J., Cendón, D.I., Rosell, L., Ortí, F., Torres Ruiz, J., Martín, J.M., Sanz, E., 2013. Salt deposition and brine evolution in the Granada Basin (late Tortonian, SE Spain). Palaeogeogr. Palaeoclimatol. Palaeoecol. 369, 452–465. https://doi.org/10.1016/j.palaeo.2012.11.010.
Gladstone, R., Flecker, R., Valdes, P., Lunt, D., Markwick, P., 2007. The Mediterranean hydrologic budget from a Late Miocene global climate simulation. Palaeogeogr. Palaeoclimatol. Palaeoecol. 251, 254–267. https://doi.org/10.1016/j.palaeo.2007.03.050.
Goldstein, R.H., 2001. Fluid inclusions in sedimentary and diagenetic systems. Lithos 55, 159–193.
Goldstein, R.H., Reynolds, T.J., 1994. Systematics of Fluid Inclusions in Diagenetic Minerals. SEPM Short Course, Tulsa, p. 199. doi:10.2110/scn.94.31.
Grant, W.D., Gemmell, R.T., McGenity, T.J., 1998. Halobacteria: the evidence for longevity. Extremophiles 2, 279–287.
Grothe, A., Andreetto, F., Reichart, G.J., Wolthers, M., Van Baak, C.G., Vasiliev, I., Stoica, M., Sangiorgi, F., Middelburg, J.J., Davies, G.R., Krijgsman, W., 2020. Paratethys pacing of the Messinian Salinity Crisis: low salinity waters contributing to gypsum precipitation? Earth Planet. Sci. Lett. 532, 116029. https://doi.org/10.1016/j.epsl.2019.116029.
Guido, A., Gerovasileiou, V., Russo, F., Rosso, A., Sanfilippo, R., Voultsiadou, E., Mastandrea, A., 2019a. Composition and biostratinomy of sponge-rich biogenic crusts in submarine caves (Aegean Sea, Eastern Mediterranean). Palaeogeogr. Palaeoclimatol. Palaeoecol. 534, 109338. https://doi.org/10.1016/j.palaeo.2019.109338.
Guido, A., Kershaw, S., Russo, F., Miriello, D., Mastandrea, A., 2019b. Application of Raman spectroscopy in comparison between cryptic microbialites of recent marine caves and Triassic patch reefs. Palaios 34 (8), 393–403. https://doi.org/10.2110/palo.2019.055.
Guido, A., Jacob, J., Gautret, P., Laggoun-Defárge, F., Mastandrea, A., Russo, F., 2007. Molecular fossils and other organic markers as palaeoenvironmental indicators of the Messinian Calcare di Base Formation: normal versus stressed marine deposition (Rossano Basin, northern Calabria, Italy). Palaeogeogr. Palaeoclimatol. Palaeoecol. 255, 265–283. https://doi.org/10.1016/j.palaeo.2007.07.015.
Guido, A., Russo, F., Miriello, D., Mastandrea, A., 2018. Autochthonous micrite to aphanodolomite: the microbialites in the dolomitization processes. Geosciences 8 (12), 451. https://doi.org/10.3390/geosciences8120451.
Guido, A., Sposato, M., Palladino, G., Vescogni, A., Miriello, D., 2022. Biomineralization of primary carbonate cements: a new biosignature in the fossil record from the Anisian of Southern Italy. Lethaia 55, 00241164. https://doi.org/10.1111/let.1245.
Guido, A., Vescogni, A., Mastandrea, A., Demasi, F., Tosti, F., Naccarato, A., Tagarelli, A., Russo, F., 2012. Characterization of the micrites in the Late Miocene vermetid carbonate bioconstructions, Salento Peninsula, Italy: Record of a microbial/metazoan association. Sed. Geol. 263–264, 133–143. https://doi.org/10.1016/j.sedgeo.2011.10.005.
Guillerm, E., Gardien, V., Ariztegui, D., Caupin, F., 2020. Restoring halite fluid inclusions as an accurate palaeothermometer: Brillouin thermometry versus microthermometry. Geostand. Geoanal. Res. 44, 243–264. https://doi.org/10.1111/ggr.12312.
Hall, D.L., Sterner, S.M., Wheeler, J.R., 1993. One-atmosphere decrepitation behavior of synthetic fluid inclusions in natural calcite: Implications for the preservation of calcite hosted inclusions during burial. Arch. Min. 49, 91–92.
Hanford, C.R., 1991. Chaper 1 marginal marine halite: Sabkhas and salinas. In: Melvin, J.L. (Ed.). In: Evaporites, Petroleum and Mineral Resources. Developments in Sedimentology, 50. Elsevier, Amsterdam, pp. 1–66.
Hoffmann, T.D., Reeksting, B.J., Gebhard, S., 2021. Bacteria- induced mineral precipitation: a mechanistic review. Microbiology 167, 001049. https://doi.org/10.1099/mic.0.001049.
Horita, J., Zimmermann, H., Holland, H.D., 2002. Chemical evolution of seawater during the Phanerozoic: Implications from the record of marine evaporites. Geochim. Cosmochim. Acta 66, 3733–3756. https://doi.org/10.1016/S0016-7037(01)00884-5.
Hovorka, S., 1987. Depositional environments of marine dominated bedded halite, Permian San Andres Formation, Texas. Sedimentology 34, 1029–1054. https://doi.org/10.1111/j.1365-3091.1987.tb00591.x.
Hovorka, S.D., Holt, R.M., Powers, D.W., 2007. Depth indicators in Permian Basin evaporites. In: Schreiber, B.C., Lugli, S., Bąbel, M. (Eds.), Evaporites Through Space and Time. The Geological Society, p. 285. https://doi.org/10.1144/SP285.19.
Hsü, K.J., Montadert, L., Bernoulli, D., Cita, M., Erickson, A., Garrison, R.E., Kidd, R.B., Mèlierés, F., Müller, C., Wright, R., 1977. History of the Mediterranean salinity crisis. Nature 267, 399–403. https://doi.org/10.1038/267399a0.
Ingram, B.L., Sloan, D., 1992. Strontium isotopic composition of estuarine sediments a paleosalinity-paleoclimate indicator. Science 255, 68–72. https://doi.org/10.1126/science.255.5040.68.
Jagniecki, E.A., Beninson, K.C., 2010. Criteria for the recognition of acid-precipitated halite. Sedimentology 57, 273–292. https://doi.org/10.1111/j.1365-3091.2009.01112.x.
Kak, C., Slaney, M., Wang, G., 2002. In: Cotellessa, R.F., Aggarwal, J.K., Wade, G. (Eds.), Principles of Computerized Tomographic Imaging.
Kiro, Y., Goldstein, S.L., Lazar, B., Stein, M., 2016. Environmental implications of salt facies in the Dead Sea. Geol. Soc. Am. Bull. 128, 824e841. https://doi.org/10.1130/B31357.1.
Krijgsman, W., Rohling, E.J., Palcu, D., Raad, F., Amarathunga, U., Flecker, R.M., Florindo, F., Roberts, A., Sierro, F.J., Aloisi, G., 2024. Causes and consequences of the Messinian salinity crisis. Nat. Rev. Earth Environ. 5 (5), 335–350. https://doi.org/10.1038/s43017-024-00533-1.
Krijgsman, W., Hilgen, F.J., Raffi, I., Sierro, F.J., Wilsonk, D.S., 1999. Chronology, causes and progression of the Messinian salinity crisis. Nature 400, 652–655. https://doi.org/10.1038/23231.
Larson, L.T., Miller, J.D., Nadeau, J.E., Roedder, E., 1973. Two sources of error in low temperature inclusion homogenization determination and corrections on published temperatures for the East Tennessee and Laisvall deposits. Econ. Geol. 68, 113–116.
Le Métayer-Levrel, G., Castanier, S., Orial, G., Loubière, J.-F., Perthuisot, J.-P., 1999. Applications of bacterial carbonatogenesis to the protection and regeneration of limestones in buildings and historic patrimony. Sediment. Geol. 126 (1–4), 25–34. https://doi.org/10.1016/S0037-0738(99)00029-9.
López-Cortés, A., Ochoa, J.-L., Vázquez-Duhalt, R., 1994. Participation of halobacteria in crystal formation and the crystallization rate of NaCl. Geomicrobiol. J. 12 (2), 69–80. https://doi.org/10.1080/01490459409377973.
Lowenstein, T.K., Hardie, L., 1985. Criteria for the recognition of salt-pan evaporites. Sedimentology 32, 627–644. https://doi.org/10.1111/j.1365-3091.1985.tb00478.x.
Lowenstein, T.K., Li, J., Brown, C.B., 1998. Paleotemperatures from fluid inclusions in halite: method verification and 100,000 year paleotemperature record, Death Valley, CA. Chem. Geol. 150, 223–245. https://doi.org/10.1016/S0009-2541(98)00061-8.
Lowenstein, T.K., Timofeeff, M.N., Brennan, S.T., Hardie, L.A., Demicco, R.V., 2001. Oscillations in Phanerozoic seawater chemistry: evidence from fluid inclusions. Science 294, 1086–1088.
Lowenstein, T.K., Schubert, B.A., Timofeeff, M.N., 2011. Microbial communities in fluid inclusions and long-term survival in halite. GSA Today 2 (1), 4–9. https://doi.org/10.1130/GSATG81A.1.
Lowenstein, T.K., Weldeghebriel, M.F., Sirota, I., Eyal, H., Mor, Z., Lensky, N.G., 2021. Criteria for the recognition of clastic halite: the modern Dead Sea shoreline. Sedimentology 68, 2253–2269. https://doi.org/10.1111/sed.12907.
Lugli, S., Dominici, R., Barone, M., Costa, E., Cavozzi, C., 2007. Messinian halite and residual facies in the Crotone basin (Calabria, Italy). In: Schreiber, B.C., Lugli, S., Babel, M. (Eds.), Evaporites Through Space and Time. Geological Society of London, vol. 285, pp. 169–178.
Lugli, S. and Lowenstein, T.K., 1997. Paleotemperatures preserved in fluid inclusions in Messinian halite, Realmonte Mine (Agrigento, Italy): Neogene Mediterranean Paleoceanography, 28–30 September 1997, Erice (Sicily), abstract volume, Societa' Geologica Italiana, Milano, Italy and ESCO Secretariat, Zurich, Switzerland, pp. 44–45.
Lugli, S., Manzi, V., Roveri, M., Schreiber, B.C., 2010. The Primary lower Gypsum in the Mediterranean: a new facies interpretation for the first stage of the Messinian salinity crisis. Palaeogeogr. Palaeoclimatol. Palaeoecol. 297, 83–99. https://doi.org/10.1016/j.palaeo.2010.07.017.
Lugli, S., Manzi, V., Roveri, M., Schreiber, B.C., 2015. The deep record of the Messinian salinity crisis: evidence of a non-desiccated Mediterranean Sea. Palaeogeogr. Palaeoclimatol. Palaeoecol. 43, 201–218. https://doi.org/10.1016/j.palaeo.2015.05.017.
Manzi, V., Lugli, S., Roveri, M., Schreiber, B.C., Gennari, R., 2011. The Messinian "Calcare die Base" (Sicily, Italy) revisited. Geol. Soc. Am. Bull. 123, 347–370. https://doi.org/10.1130/B30262.1.
Mahmoud, S., Wahed, M.A., Mohamed, E.A., El-sayed, M.I., M'nif, A., Sillanpää, M., 2015. Hydrogeochemical processes controlling the water chemistry of a closed saline lake located in Sahara Desert: Lake Qarun, Egypt. Aquat. Geochem. 21 (1), 31–57.
Manzi, V., Lugli, S., Roveri, M., Schreiber, C.B., 2009. A new facies model for the Upper Gypsum of Sicily (Italy): Chronological and palaeoenvironment constraints for the Messinian salinity crisis in the Mediterranean. Sedimentology 56, 1937–1960. https://doi.org/10.1111/j.1365-3091.2009.01063.x.
McArthur, J.M., Howarth, R.J., Shields, G.A., 2012. Strontium isotope stratigraphy. In: Gradstein, F.M., Ogg, J.G., Schmitz, M.D., Ogg, G.M. (Eds.), The Geological Time Scale 2012. Elsevier B.V, Oxford, pp. 127–144.
McGenity, T.J., Gemmell, R.T., Grant, W.D., Stan-Lotter, H., 2000. Origins of halophilic microorganisms in ancient salt deposits: Minireview. Environ. Microbiol. 2 (3), 243–250. https://doi.org/10.1046/j.1462-2920.2000.00105.x.
Müller, D.W., Mueller, P.A., 1991. Origin and age of the Mediterranean Messinian evaporites: implications form Sr isotopes. Earth Planet. Sci. Lett. 107, 1–12. https://doi.org/10.1016/0012-821X(91)90039-K.
Natalicchio, M., Dela Pierre, F., Lugli, S., Lowenstein, T.K., Feiner, S.J., Ferrando, S., Manzi, V., Roveri, M., Clari, P., 2014. Did late Miocene (Messinian) gypsum precipitate from evaporated marine brines? Insights from the piedmont basin (Italy). Geology 42, 179–182. https://doi.org/10.1130/G34986.1.
Natalicchio, M., Pellegrino, L., Clari, P., Pastero, L., Dela Pierre, F., 2021. Gypsum lithofacies and stratigraphic architecture of a Messinian marginal basin (Piedmont Basin, NW Italy). Sed. Geol. 425, 106009. https://doi.org/10.1016/j.sedgeo.2021.106009.

Ohneiser, C., Florindo, F., Stocchi, P., Roberts, A.P., DeConto, R.M., Pollard, D., 2015. Antarctic glacio-eustatic contributions to late Miocene Mediterranean desiccation and reflooding. Nat. Commun. 6, 8765. https://doi.org/10.1038/ncomms9765.

Otsu, N., 1979. A threshold selection method from gray-level histograms. IEEE Trans. Syst. Man Cybern 9, 62–66.

Paganin, D., Mayo, S.C., Gureyev, T.E., Miller, P.R., Wilkins, S.W., 2002. Simultaneous phase and amplitude extraction from a single defocused image of a homogeneous object. J. Microsc. 206, 33–40. https://doi.org/10.1046/j.1365-2818.2002.01010.x.

Perri, F., Dominici, R., Guido, A., Cipriani, M., Cianflone, G., 2023. Geochemistry of mudrocks from the Calcare di Base Formation (Catanzaro Basin, Calabria): preliminary data. Rend. Online Soc. Geol. It. 59, 71–74. https://doi.org/10.3301/ROL.2023.11.

Perri, F., Guido, A., Cipriani, M., Cianflone, G., Dominici, R., 2024. Geochemical and mineralogical proxies from the Messinian mudrocks (Catanzaro Basin, southern Italy): Paleoweathering and paleoclimate evolution during the onset of the Messinian salinity Crisis. Mar. Pet. Geol. 163, 106703. https://doi.org/10.1016/j.marpetgeo.2024.106703.

Pironon, J., Pagel, M., Lévêque, M.H., Mogé, M., 1995. Organic inclusions in salt. Part I: Solid and liquid organic matter, carbon dioxide and nitrogen species in fluid inclusions from the Bresse basin (France). Org. Geochem. 23 (5), 391–402.

Reinhardt, E.G., Stanley, D.J., Patterson, R.T., 1998. Strontium paleontological method as a highresolution paleosalinity tool for lagoonal environments. Geology, 26, 1003-1006. In: Briand, F., Monaco (Eds.), 33ème CIESM Workshop Monographs. 33, 91–96.

Reynolds, C.S., Huszar, V., Kruk, C., Naselli-Flores, L., Melo, S., 2002. Towards a functional classification of the freshwater phytoplankton. J. Plankton Res. 24, 417–428.

Rigaudier, T., Lécuyer, C., Gardien, V., Jean-Pierre Suc, Martineau, F., 2011. The record of temperature, wind velocity and air humidity in the dD and $d^{18}O$ of water inclusions in synthetic and Messinian halites. Geochim. Cosmochim. Acta 75, 4637–4652.

Rivers, M., 1998. Tutorial Introduction to X-Ray Computed Microtomography Data Processing. University of Chicago.

Roberts, S.M., Spencer, R.J., 1995. Paleotemperatures preserved in fluid inclusions in halite. Geochim. Cosmochim. Acta 59 (19), 3929–3942. https://doi.org/10.1016/0016-7037(95)00253-V.

Roda, C., 1964. Distribuzione e facies dei sedimenti Neogenici nel Bacino Crotonese. Geol. Rom. 3, 319–366.

Roedder, E., 1984. Fluid inclusion. Rev. Mineral. 12, 11–45.

Roveri, M., Bertini, A., Cosentino, D., Di Stefano, A., Gennari, R., Gliozzi, E., Grossi, F., Iaccarino, S.M., Lugli, S., Manzi, V., Taviani, M., 2008a. A high-resolution stratigraphic framework for the latest Messinian events in the Mediterranean area. Stratigraphy 5 (3–4), 323–342.

Roveri, M., Lugli, S., Manzi, V., Gennari, R., Schreiber, B.C., 2014. High-resolution strontium isotope stratigraphy of the Messinian deep Mediterranean basins: Implications for marginal to central basins correlation. Mar. Geol. 359, 113–125. https://doi.org/10.1016/j.margeo.2014.01.002.

Roveri, M., Lugli, S., Manzi, V., Schreiber, B.C., 2008b. The Messinian Sicilian stratigraphy revisited: new insights for the Messinian salinity crisis. Terra Nova 20 (6), 483–488. https://doi.org/10.1111/j.1365-3121.2008.00842.x.

Sankaranarayanan, K., Timofeeff, M.N., Spathis, R., Lowenstein, T.K., Lum, J.K., 2011. Ancient microbes from halite fluid inclusions: optimized surface sterilization and DNA extraction. PLoS One 6 (6), e20683. https://doi.org/10.1371/journal.pone.0020683.

Schildgen, T.F., Cosentino, D., Frijia, G., Castorina, F., Dudas, F.O., Iadanza, A., Sampalmieri, G., Cipollari, P., Caruso, A., Bowring, S.A., Strecker, M.R., 2014. Sea level and climate forcing of the Sr isotope composition of Late Miocene Mediterranean marine basins. Geochem. Geophys. Geosyst. 15, 2964–2983. https://doi.org/10.1002/2014GC005332.

Schléder, Z., Urai, J.L., 2005. Microstructural evolution of deformation-modified primary halite from the Middle Triassic Röt Formation at Hengelo, the Netherlands. Int. J. Earth Sci. 94, 941–955. https://doi.org/10.1007/s00531-005-0503-2.

Schreiber, B.C., Hsü, H.J., 1980. Evaporites. In: Hobson, G.D. (Ed.), Developments in Petroleum Geology-2. Applied Sci. Pub, Barkng, Essex, England, pp. 87–138.

Schubert, B.A., Lowenstein, T.K., Timofeeff, M.N., 2009. Microscopic identification of prokaryotes in modern and ancient halite, Saline Valley and Death Valley, California. Astrobiology 9, 467–482. https://doi.org/10.1089/ast.2008.0282.

Schubert, B.A., Timofeeff, M.N., Lowenstein, T.K., Polle, J.E.W., 2010a. Dunaliella cells in fluid inclusions in halite: significance for long-term survival of Prokaryotes. Geomicrobiol J. 26, 61–75. https://doi.org/10.1080/01490450903232207.

Schubert, B.A., Lowenstein, T.K., Timofeeff, M.N., Parker, M.A., 2010b. Halophilic Archea cultures from ancient halite, Death Valley, California. Environ. Microbiol. 12 (2), 440–454. https://doi.org/10.1111/j.1462-2920.2009.02086.x.

Shepherd, T., Rankin, A.H., Alderton, D.H.M., 1985. A practical guide of fluid inclusions studies. Blackie & Son Limited, Glasgow, p. 239.

Sirota, I., Enzel, Y., Lensky, N.G., 2017. Temperature seasonality control on modern halite layers in the Dead Sea: In situ observations. Geol. Soc. Am. Bull. 129 (9–10), 1181–1194. https://doi.org/10.1130/B31661.1.

Southgate, P.N., 1982. Cambrian skeletal halite crystals and experimental analogues. Sedimentology 29, 391–407.

Speranza, G., Cosentino, D., Tecce, F., Faccenna, C., 2013. Paleoclimate reconstruction during the Messinian evaporative drawdown of the Mediterranean Basin: Insights from microthermometry on halite fluid inclusions. Geochem. Geophys. Geosyst. 14, 5054–5077. https://doi.org/10.1002/2013GC004946.

Speranza, G., Vona, A.l., Vinciguerra, S., Omano, C., 2016. Relating natural heterogeneities and rheological properties of rocksalt: New insights from microstructural observations and petrophyisical parameters on Messinian halites from the Italian Peninsula. Tectonophysics 666, 103–120. https://doi.org/10.1016/j.tecto.2015.10.018.

Sterner, S.M., Hall, D.L., Bodnar, R.J., 1988. Synthetic fluid inclusions. V. Solubility relations in the system NaCl-KCl-H_2O under vapor-saturated conditions. Geochim. Cosmochim. Acta 52, 989–1005. https://doi.org/10.1016/0016-7037(88)90254-2.

Taj, R.J., Aref, M.A., 2015. Structural and textural characteristics of surface halite crusts of a supratidal, ephemeral halite pan, South Jeddah, Red Sea Coast, Saudi Arabia. Facies 61, 2. https://doi.org/10.1007/s10347-014-0426-0.

Topper, R.P.M., Flecker, R., Meijer, P.T., Wortel, M.J.R., 2011. A box model of the Late Miocene Mediterranean Sea: implications from combined $^{87}Sr/^{86}Sr$ and salinity data. Paleoceanography 26, PA3223. https://doi.org/10.1029/2010PA002063.

Topper, R.P.M., Meijer, P.T., 2013. A modelling perspective on spatial and temporal variations in Messinian evaporite deposits. Mar. Geol. 336, 44–60. https://doi.org/10.1016/j.margeo.2012.11.009.

Toscani, L., Venturelli, G., Barbieri, M., Capedri, S., Fernandez, J.M., Oddone, M., 1990. Geochemistry and petrogenesis of two-pyroxene andesites from Sierra de Gata, SE Spain. Mineral. Petrol. 41, 199–213.

Urai, J.L., Spiers, C.J., 2007. The effect of grain boundary water on deformation mechanisms and rheology of rocksalt during long-term deformation. In: Wallner, M., Lux, K.-H., Minkly, W., Hardy, H.R. (Eds.), The Mechanical Behaviour of Salt-Understanding of THMC Processes in Salt Rocks: 6th Conference (SaltMech6). Taylor & Francis, Hannover, Germany, p. 10.

Van Dijk, J.P., Bello, M., Brancaleoni, G.P., Cantarella, G., Costa, V., Frixa, A., Golfetto, F., Merlini, S., Riva, M., Torricelli, S., Toscano, C., Zerilli, A., 2000. A regional structural model for the northern sector of the Calabrian Arc (southern Italy). Tectonophysics 324, 267–320. https://doi.org/10.1016/S0040-1951(00)00139-6.

Vespasiano, G., Marini, L., Muto, F., Auque, L.F., De Rosa, R., Jimenez, J., Gimeno, M.J., Pizzino, L., Sciarra, A., Cianflone, G., Cipriani, M., Guido, A., Fuoco, I., Barca, D., Dotsika, E., Bloise, A., Apollaro, C., 2023. A multidisciplinary geochemical approach to geothermal resource exploration: the Spezzano Albanese thermal system, southern Italy. Mar. Pet. Geol. 155, 106407. https://doi.org/10.1016/J.Marpetgeo.2023.106407.

Vespasiano, G., Marini, L., Muto, F., Auquéc, L.F., Cipriani, M., De Rosa, R., Critelli, S., Gimeno, M.J., Blasco, M., Dotsika, E., Apollaro, C., 2021. Chemical, isotopic and geotectonic relations of the warm and cold waters of the Cotronei (Ponte Coniglio), Bruciarello and Repole thermal areas, (Calabria - Southern Italy). Geothermics 96, 102228. https://doi.org/10.1016/j.geothermics.2021.102228.

Vidal, L., Bickert, T., Wefer, G., Röhl, U., 2002. Late Miocene stable isotope stratigraphy of SE Atlantic ODP site 1085: Relation to Messinian events. Mar. Geol. 180 (1–4), 71–85. https://doi.org/10.1016/S0025-3227(01)00206-7.

Vityk, O.M., Bodnar, R.J., Doukhan, J.C., 2000. Synthetic fluid inclusions. XV. TEM investigation of plastic flow associated with reequilibration of fluid inclusions in natural quartz. Contrib. Miner. Petrol. 139 (3), 285–297.

Vreeland, R.H., Sun, Y.P., Wang, B.B., Hou, J., Cui, H.L., 2024. Halorubrum hochsteinianum sp. nov., an ancient haloarchaeon from a natural experiment. Extremophiles 28, 1. https://doi.org/10.1007/s00792-023-01320-4.

Warren, J.K., 1999. Evaporites. their evolution and economics. Geol. Mag. 137 (4), 463–479.

Warren, J.K., 2006. Evaporites: Sediments, Resources and Hydrocarbons. Springer Berlin, Heidelberg, p. 1036.

Wierzchos, J., Ascaso, C., Mckay, C.P., 2006. Endolithic cyanobacteria in halite rocks from the hyperarid core of the Atacama desert. Astrobiology 6 (3), 415–422.

Zecchin, M., Civile, D., Caffau, M., Critelli, S., Muto, F., Mangano, G., Ceramicola, S., 2020. Sedimentary evolution of the Neogene-Quaternary Crotone Basin (southern Italy) and relationships with large-scale tectonics: a sequence stratigraphic approach. Mar. Pet. Geol. 117, 104381. https://doi.org/10.1016/j.marpetgeo.2020.104381.

Zhang, W., Hu, Z., 2020. Estimation of isotopic reference values for pure materials and geological reference materials. At. Spectrosc. 41 (3), 93–102. https://doi.org/10.46770/AS.2020.03.001.